Published in final edited form as:
Nat Immunol. 2021 October ; 22(10): 1280–1293. doi:10.1038/s41590-021-01012-1.

Antimicrobial immunity impedes CNS vascular repair following brain injury

Panagiotis Mastorakos[1,2], **Mathew V. Russo**[1], **Tianzan Zhou**[1], **Kory Johnson**[3], **Dorian B. McGavern**[1]

[1]Viral Immunology & Intravital Imaging Section, National Institute of Neurological Disorders and Stroke, National Institutes of Health, Bethesda, Maryland

[2]Department of Surgical Neurology, National Institute of Neurological Disorders and Stroke, National Institutes of Health, Bethesda, Maryland

[3]National Institute of Neurological Disorders and Stroke, National Institutes of Health, Bethesda, MD

Abstract

Traumatic brain injuries (TBI) and cerebrovascular injuries are leading causes of disability and mortality worldwide. Systemic infections often accompany these disorders and can worsen outcomes. Recovery after brain injury depends on innate immunity, but the effect of infections on this process is not well understood. Here, we demonstrate that systemically introduced microbes and microbial products interfered with meningeal vascular repair after TBI in a type I interferon (IFN-I)-dependent manner, with sequential infections promoting chronic disrepair. Mechanistically, we discovered that MDA5-dependent detection of an arenavirus encountered after TBI disrupted pro-angiogenic myeloid cell programming via induction of IFN-I signaling. Systemic viral infection similarly blocked restorative angiogenesis in the brain parenchyma after intracranial hemorrhage, leading to chronic IFN-I signaling, blood brain barrier leakage and a failure to restore cognitive-motor function. Our findings reveal a common immunological mechanism by which systemic infections deviate reparative programming after CNS injury and offer a new therapeutic target to improve recovery.

Introduction

Traumatic brain injury (TBI) and cerebrovascular injury (CVI) are the two most common causes of acquired brain injury and are major contributors to death and disability

---

Corresponding Author: Dorian B. McGavern, Ph.D., National Institutes of Health, Building 10, Room 5N240C, Bethesda, MD 20892, mcgavernd@mail.nih.gov, Phone: 301-443-7949.

Author Contributions Statement

P.M., M.V.R. and TZ performed the design, data acquisition and analysis. K.J. conducted computation analyses of RNA-seq data. P.M. and D.B.M. wrote and edited the manuscript. D.B.M. supervised and directed the project and participated in experimental design, data acquisition and analysis.

Competing Interests Statement

The authors declare no financial or non-financial competing interests.

worldwide[1]. Despite the negative impact of these injuries on human health, treatment is limited to reperfusion strategies, management of intracranial pressure, and supportive measures[2,3]. Disease modifying agents to minimize secondary injury and promote repair are lacking. Moreover, patients with brain injuries have differential recovery trajectories that are not completely understood. TBI and CVI are strongly associated with neurodegeneration, and development of dementia following these injuries is attributed partly to chronic inflammation and failure to restore central nervous system (CNS) barriers[4,5]. A better understanding of factors that influence CNS repair following brain injury is required to design therapies that improve long-term outcomes.

Systemic infections are commonly observed following TBI and CVI, especially in hospitalized patients[6–9], and most occur within a week of injury[7]. The increased risk of infection is often attributed to systemic immunosuppression[10,11]. Systemic infections following TBI[12–14] and CVI[6,8,15] have been associated with poor short- and long-term outcomes as well as increased mortality, and antibiotics have failed to reduce infection rates or improve associated outcomes[16]. It is known that bacteremia can slow peripheral wound healing[17,18], but the influence of infections on CNS repair is not well understood.

The CNS has an elaborate barrier system, specialized vasculature, and neural networks that can all become damaged by brain injuries[19]. Such injuries are variable in nature and can be associated with meningeal damage, barrier leakage, hemorrhage, brain swelling, cell death, inflammation, etc. Prolonged barrier leakage can induce a chronic state of secondary cell death and inflammation[20,21]. Therefore, rapid restoration of CNS barriers is essential for recovery after injury, and the effect of systemic infections on this process is not well defined.

The immune system plays a crucial role in mediating repair following injury[22,23] and can become distracted by infections. CNS resident as well as peripheral myeloid cells mobilize in response CNS injuries. These cells fortify the vasculature and glia limitans and contribute to dead cell removal, angiogenesis, and tissue remodeling[24–27]. Reparative immune programming is coordinated temporally and spatially[25–27], making it susceptible to deviation or delay[26–28]. Because antimicrobial and wound-healing responses utilize common cells of the immune system, infections encountered after a brain injury have the potential to interrupt reparative programming[23,29,30].

Because TBI and CVI patients often encounter infections that may disrupt repair, we set out to identify mechanisms by which systemic infections alter immune-mediated reparative programming in the meninges and brain parenchyma after injury. We introduced diverse pathogens and pathogen-associated molecular patterns (PAMPs) into the periphery that all interfered with repair of damaged CNS vasculature. To gain more in-depth mechanistic insights into this process, we decided to focus on how peripheral infection with lymphocytic choriomeningitis virus (LCMV) Armstrong, a noncytopathic arenavirus, disrupted the CVI and TBI repair trajectories. These studies uncovered an important role for the type I interferon (IFN-I) system in reprogramming CNS wound-healing following systemic infection.

Results

Infection impairs meningeal vascular repair after mild TBI

To assess the effect of systemic infection on repair, we first established a precise timeline of meningeal vascular repair kinetics following mild TBI (mTBI). We used our previously established mTBI model that involves compression of the meningeal space. This injury induces cellular death and vascular injury in the meninges as well as damage to glial limitans and brain parenchyma[25,26]. To quantify meningeal vascular integrity and function, we injected fluorescent tomato lectin intravenously (i.v.) at different time points post-injury and then stained meningeal whole mounts immunohistochemically to visualize laminin. Tomato lectin labels healthy vascular endothelium and serves as an indicator of functional blood vessels, whereas laminin staining identifies both functional and non-functional vascular structures. Following initial mTBI-induced meningeal damage meninges at day 1, the lesion steadily revascularized over the ensuing week (Fig. 1a,b). As described previously[26], the new vascular network consisted of small loops that are easily distinguished from surrounding uninjured vasculature (Fig. 1a).

Having established repair kinetics, we next determined how different systemic infections influenced the meningeal repair trajectory. As a representative, we administered lymphocytic choriomeningitis virus (LCMV) Armstrong, noncytopathic RNA virus, i.v. four days after mTBI. LCMV infection significantly impaired meningeal vascular repair, resulting in revascularization of only 23.1 ± 6.6% of the lesion at day 7 post-mTBI relative to near complete repair observed in uninfected mice (Fig. 1c,d). This impairment was not observed in LCMV carrier mice[31,32] persistently infected from birth with the virus (Fig 1i). Carrier mice have LCMV distributed throughout every tissue and are immunologically tolerant to the virus[32]. The normal meningeal repair observed in carrier mice indicates that LCMV itself is not responsible for the disruption that occurs following acute LCMV infection.

To evaluate another viral paradigm, we infected mice intranasally with vesicular stomatitis virus (VSV) Indiana one day prior to mTBI. VSV administered intranasally is known to infect nasal neuroepithelium and then travel caudally into the olfactory bulb via olfactory sensory neuron projections[33]. Intranasal VSV infection reduced repair to 37.7 ± 8.8% of the lesion over 7 days. To determine if decreased meningeal repair was due to viral replication or recognition of pathogen-associated molecular patterns (PAMPs), we administered polyI:C systemically on day 4 post-injury. PolyI:C is a synthetic analog of double-stranded RNA that activates antiviral PAMP receptors. PolyI:C impeded repair of meningeal vasculature after mTBI but not as much as intact virus (Fig. 1c,d). Collectively, these data demonstrate that both viruses and viral PAMPs are detrimental to the meningeal repair process.

To assess non-viral infections and PAMPs, we systemically administered the pathogenic yeast *Candida albicans* (a representative fungal infection) or *lipopolysaccharides* (LPS) from *Escherichia coli* O55:B5 (a surrogate for bacterial infection) on day 4 post-mTBI. *C. albicans* infection and LPS administration both reduced repair to 66.3 ± 4.1% (Fig. 1e,f) and 66.3 ± 4.1% of the lesion (Fig. 1g,h), respectively. Our results indicate that a broad range of systemic pathogens / PAMPs can impair meningeal revascularization following mTBI.

Viral infection alters angiogenic programming

We next sought to determine how a systemic viral infection influenced these aspects of lesion repair. Angiogenic programming was assessed by quantifying expression of 90 angiogenesis-related genes in small punch biopsies containing lesioned meninges and superficial neocortex (see Supplementary Table 1 for complete list of genes). These biopsies were obtained from uninfected and LCMV-infected mice 5 days after mTBI. LCMV was introduced i.v. into the infected mouse group on day 4. The data revealed that LCMV infection altered angiogenic pathways, markedly decreasing expression of five angiogenesis-related genes (*Cxcl12, Cyr61, Fn1, Thbs1, Vegfa, Pdgfrb, Angpt2*) and increasing expression of three genes (*Ang, TNfrsf12a, Epha2*) (Fig. 1j,k; Supplementary Table 1).

Viral infection alters the reparative macrophage distribution

We showed previously that angiogenesis is induced in the meninges following mTBI and that the lesion distribution of macrophages derived from classical versus non-classical monocytes is important for the reparative process[26]. We examined whether LCMV influenced the distribution of mTBI lesion macrophages known to facilitate angiogenesis. By first conducting a time course in uninfected mice, we confirmed that CD11b$^+$CD206$^-$ inflammatory macrophages gradually accumulate in the meningeal lesion core within 5 days of mTBI, whereas CD11b$^+$CD206$^+$ wound-healing macrophages localize more so to the lesion perimeter (Fig. 2a). LCMV infection significantly altered this macrophage distribution pattern on day 5, impeding the accumulation of CD11b$^+$CD206$^-$ macrophages within the mTBI lesion core (Fig. 2b–d). These cells were instead retained in the lesion perimeter where they comingled with an elevated number of CD11b$^+$CD206$^+$ macrophages. Collectively, these data demonstrate that a systemic viral infection can disrupt the meningeal lesion macrophage distribution and angiogenic programming within 24 hours of inoculation.

Secondary infection promotes a prolonged state of disrepair

We demonstrated that systemic viral infection was able to disrupt a meningeal repair process, but it was unclear whether this was a permanent block or a delay in repair. To address this question, we infected mTBI mice with LCMV on day 4 and then assessed meningeal repair on days 7 and 30 post-injury. Relative to uninfected controls, LCMV-infected mice had 39 ± 2.4% repair at day 7, but this progressed to 92.3 ± 0.9% repair by day 30 (Fig. 3a,b), indicating that infected mice can eventually repair over time. Given the slower repair kinetics in injured mice following acute infection, we next evaluated the impact of a secondary infection. We infected mTBI mice with LCMV on day 4 and then introduced a homologous (i.v. LCMV) or heterologous (intranasal VSV) challenge on day 10. As expected, due to pre-existing immunity, infection with LCMV on day 4 and then again on day 10 had no additional effect on the meningeal repair process relative to a single infection on day 4 (Fig. 3c–e). These mice showed near complete meningeal revascularization on days 14 and 30 post-injury. By contrast, mice exposed to i.v. LCMV on day 4 followed by intranasal VSV on day 10 had only 50 ± 6.8% lesion repair at day 14 and 60.4 ± 4.7% lesion repair at day 30 (Fig. 3C–E). These data demonstrate that exposure to a secondary infection can further impede the meningeal repair process following mTBI.

Viral infection induces a IFN-I response

We next explored the antiviral immune response that developed in the context of mTBI and how this might influence reparative programming. IFN-I's are known to facilitate innate and adaptive immune reactions against diverse microbes, including LCMV[34]. We used real-time quantitative PCR (qPCR) to quantify expression of known IFN-I's and downstream interferon-stimulated genes (ISGs) in meningeal / superficial neocortex biopsies acquired from the lesion of uninfected and infected mTBI mice (see Supplementary Table 1 for a complete list of genes). Mice that received a mTBI were infected i.v. on day 4 with LCMV and then analyzed on day 5 (TBI d5 + LCMV). IFN-I and ISG expression were compared to uninfected/uninjured mice (Ctrl), uninfected mice day 1 (TBI d1) and day 5 (TBI d5) after mTBI as well as LCMV-infected mice on day 1 (LCMV d1) and day 5 (LCMV d5) after infection. We quantified the expression of 14 different type I interferons and detected a marked increase in all species only in mTBI mice infected with LCMV (Fig. 3f; Supplementary Table 1). Quantification of 79 ISGs in the same groups of mice uncovered two distinct expression patterns (Fig. 3g; Supplementary Table 1). Five days following mTBI, the ISG expression pattern was defined by a cluster of genes that included *Jak2*, *Tyk2*, *Irf1*, *Stat3* and *Tlr3*, among others. By contrast, LCMV-infected mTBI mice at day 5 expressed a different and broader pattern of ISGs that included high levels of *Stat1*, *Stat2*, *Ifit1*, *Ifit3*, and *Oas1b*. These data indicate that LCMV induces a potent IFN-I response in injured mice that dramatically shifts the ISG expression pattern relative to their uninfected counterparts.

Interferon signaling in myelomonocytic cells impedes repair

Given the differential IFN-I response in uninfected vs. infected mTBI mice, we evaluated the impact of this signaling on meningeal repair. This was first accomplished by studying IFN-I receptor (IFNAR) deficient mice. Uninfected wild type and IFNAR$^{-/-}$ mice were able to similarly repair meningeal vasculature 7 days following mTBI (Fig. 4a), indicating that IFNAR-mediated signaling is not required for the normal repair process. However, IFNAR deficiency completely rescued meningeal repair in LCMV-infected mTBI mice (Fig. 4a). These mice showed a repair level comparable to that observed in uninfected controls. A similar result was obtained when mice were injected intraperitoneally with an αIFNAR-blocking antibody on day 3 post-mTBI – one day prior to LCMV infection on day 4 (Fig. 4b). Treatment with αIFNAR-blocking antibody also improved repair in mice exposed to LPS or *Candida albicans* (Extended Data Fig. 1). Collectively, these data demonstrate the importance of IFNAR signaling in blocking meningeal repair after infection.

We next sought insights into the relevant cell population(s) modulated by infection-induced IFNAR signaling. We demonstrated previously that peripheral myeloid cells are required for meningeal repair following mTBI[26]. We therefore generated floxed IFNAR mice expressing Cre recombinase under control of the lysozyme M promoter (LysM$^{cre/+}$IFNAR$^{fl/fl}$). These mice allowed us to assess whether IFNAR signaling in peripheral myelomonocytic cells was responsible for faulty meningeal repair. Importantly, deletion of IFNAR from myelomonocytic cells resulted in complete restoration of meningeal repair on day 7 in LCMV-infected mTBI mice (Fig. 4C). These data supported the conclusion that IFN-I signaling in myelomonocytic cells was responsible for the reparative defect seen in infected mTBI mice.

MDA5-mediated sensing is required to block meningeal repair

To further explore the mechanism by which viral infection impeded repair, we evaluated a step preceding IFN-I and ISG induction. We specifically addressed whether innate detection of LCMV was required for the meningeal repair impediment. Melanoma-differentiation-associated gene 5 (MDA5) is a RIG-I-like receptor dsRNA helicase enzyme that functions as a pattern recognition receptor and can detect viruses like LCMV[35]. We infected MDA5-deficient mice at day 5 post-mTBI and evaluated meningeal repair on day 7. Relative to wild type LCMV-infected controls, repair of meningeal vasculature was almost fully restored at day 7 post-mTBI in MDA5$^{-/-}$ mice (Fig. 4d,e). We then assessed whether the pattern of IFN-I and ISG expression observed in LCMV-infected mTBI mice was influenced by MDA5 deficiency. IFN-I and ISG expression in the damaged meninges and neocortex was quantified on day 5 post-mTBI in wild type and MDA5$^{-/-}$ mice – one day following i.v. infection with LCMV on day 4 (Fig. 4f,g). Uninfected mTBI mice were also processed as a control for this experiment. Importantly, MDA5 deficiency reduced expression of all LCMV-induced IFN-I's to levels observed in uninfected mTBI mice (Fig. 4f). Moreover, ISG expression was markedly reduced relative to wild type LCMV-infected mice and to levels often below that observed in uninfected controls (Fig. 4g). The few upregulated genes (*Ccl2*, *Ccl4*, *Crp*, *H2-M10.1*) detected in MDA-5$^{-/-}$ mice appeared to have no impact on meningeal repair. These data demonstrate that innate recognition of LCMV via MDA5 is required to initiate IFN-I dependent disruption of meningeal repair.

Transcranial IFN-β1 administration impairs meningeal vascular

Given the role of MDA-5 and IFN-I in disrupting meningeal repair, we next focused on whether IFN-I alone could mediate this effect and whether signaling needed to occur locally or systemically. This was accomplished by administering IFN-β1 locally or systemically to mTBI mice on days 5 and 6 post-injury. For systemic administration IFN-β1 was injected i.v., whereas it was applied transcranially through the thinned skull bone for the local application. Quantification of meningeal repair on day 7 post-mTBI revealed that intravenous and transcranial administration of IFN-β1 reduced repair to 63.2 ± 1.9% and 74.6 ± 7.3%, respectively (Fig. 5a,b). LCMV-infected controls in this experiment showed 43.6 ± 3.7% repair, whereas uninfected mTBI mice had near complete meningeal repair (99 ± 0.9%). To further interrogate whether systemic or local IFN-I was required to impede repair, we created a model of bilateral mTBI lesions and administered IFN-β1 transcranially to only one of the two lesions (ipsilateral). In this experiment, the ipsilateral IFN-β1-treated lesion demonstrated only 59.4 ± 4.3% repair, whereas the vehicle control-treated contralateral lesion had 92.2 ± 4.1% repair (Fig. 5c,d). From these data, we conclude that IFN-β1 acting locally within the mTBI lesion phenocopies the detrimental effect that systemic LCMV infection has on meningeal repair.

To determine how IFN-β1 disrupted the reparative process, we conducted an intravital two-photon imaging study in CX3CR1$^{gfp/+}$CCR2$^{rfp/+}$ mice to examine peripheral myeloid cell lesion dynamics following transcranial application of IFN-β1. CX3CR1$^{gfp/+}$CCR2$^{rfp/+}$ mice received a mTBI and were then incubated transcranially with IFN-β1 or vehicle for 1 hour. Myeloid cell dynamics in the lesion and peri-lesion area were filmed for an additional hour by intravital two-photon microscopy. Transcranial IFN-β1 markedly enhanced recruitment of CCR2$^+$ monocytes relative to the vehicle control group and promoted their movement into the peri-lesion area (Fig. 5e,f; Video 1). These data demonstrate that IFN-β1 alone (without infection) can alter the local distribution of peri-lesion myeloid cells following mTBI.

IFN-I impairs brain parenchymal angiogenesis

Because IFN-I triggered by viral infection was able to disrupt meningeal angiogenesis following mTBI, we became interested in whether repair of other CNS vasculature was similarly disrupted by an infection. For example, vasculature within the brain parenchyma can be damaged by stroke, TBI, or intracranial hemorrhage, requiring immune-mediated angiogenesis to restore function[36,37]. We recently developed a model of isolated cerebrovasculature injury (CVI) that involves application of low intensity pulsed ultrasound through a thinned skull window of mice injected i.v. with microbubbles[27]. This approach causes immediate cerebrovascular damage and hemorrhage in the parenchyma beneath the thinned skull window, which is followed by immune-mediated vascular remodeling. We evaluated the impact of viral infection on vascular repair in the brain parenchyma by challenging mice i.v. on day 4 post-CVI with LCMV. We showed previously in this model that cerebrovasculature is rebuilt by day 10 post-injury[27]. We therefore identified cerebrovasculature with fluorescent tomato lectin / laminin staining and quantified the extent of parenchymal vascular coverage in uninfected vs. infected mice at day 10 post-CVI. At this time point, we observed development of new vessels in uninfected CVI mice. These vessels had an irregular distribution, increased diameter and increased density as described previously (Fig. 6a)[27]. However, neo-vascular coverage was markedly reduced 25.1-fold in LCMV-infected mice relative to controls (Fig. 6a,b), demonstrating that viral infection can impede angiogenesis in the parenchyma similar to the meninges.

To determine if the IFN-I system was involved in blocking parenchymal repair following CVI, we compared vascular coverage in LCMV-infected wild type vs. MDA5$^{-/-}$ mice (Fig. 6c). Complete restoration of vascular repair was observed in infected MDA5$^{-/-}$ mice on day 10 post-CVI. In fact, the repair level was comparable to that seen in uninfected wild type controls (Fig. 6c). Similarly, full restoration of vascular repair was observed in LCMV-infected IFNAR$^{-/-}$ mice; however, deletion of IFNAR from myelomonocytic cells in LysM$^{cre/+}$IFNAR$^{fl/fl}$ mice only achieved partial restoration of repair (Fig. 6d,e), suggesting disruption of another cell population by IFN-I signaling. Collectively, these data indicate that LCMV infection impedes cerebrovascular repair in a MDA5, IFN-I dependent manner, but that interferon signaling is required in cells other than just myelomonocytic cells to achieve the full defect.

Viral infection following CVI promotes neuronal loss

To define other pathological consequences (if any) associated with failed revascularization after LCMV infection, we examined neocortical anatomy in uninfected versus infected mice at day 10 post-CVI. Confocal imaging of the brain parenchyma in LCMV-infected mice at this time point revealed a notable lack of Tomato-lectin$^+$ blood vessels as well as some abnormal vascular structures (Fig. 6f). These regions of damaged neocortex also showed a considerable loss of NeuN$^+$ neurons (5.9-fold when compared to uninfected controls) and an increase in Iba1$^+$ myeloid cells (0.6-fold increase) (Fig. 6f–h). These results indicate that viral infection following CVI not only impedes angiogenesis but also promotes neuronal loss and myeloid cell accumulation.

Viral infection following CVI promotes sustained BBB breakdown

We also assessed the impact of infection on BBB breakdown and recovery after CVI. Analysis of axial sections from the neocortex of mice at day 10 post-CVI revealed that LCMV infection on day 4 significantly enhanced Evans blue leakage and the extent of glial fibrillary acidic protein (GFAP)$^+$ gliosis relative to uninfected controls (Fig. 7a–c). Further analysis of BBB leakage kinetics by fluorometry uncovered that the BBB resealed in uninfected mice by day 10 post-CVI (Fig. 7d). By contrast, enhanced BBB leakage was observed on day 5 (one day following LCMV infection), and this leakage persisted until day 20 when compared to uninfected controls. At this time point, a reduction in vascular tight junction proteins (claudin-5 and ZO-1) was observed in previously infected mice relative to controls (Extended Data Fig. 2). These data demonstrate that viral infection during the CVI-induced repair process promotes a persistent state of BBB leakage and increased GFAP$^+$ astrocytes.

Infection promotes IFN-I signaling and cognitive dysfunction after CVI

Repair of damaged CNS tissue after injury represents an attempt to reestablish steady state functionality and gene expression. To better understand how an infection encountered early during the reparative process might deviate the return to homeostasis, we analyzed gene expression in the neocortex by RNAseq at day 20 post-CVI (uninfected vs. infected) relative to uninjured controls. We selected this time point because our previous study showed that CVI mice regain neurological function and relatively normal gene expression in the neocortex by day 20[27]. Comparison of gene expression patterns using a Pearson correlation-based clustered heat map revealed clustering of samples into three distinct groups with clear differences in expression profiles (Fig. 8a). Principal component analysis (PCA) based on 94.2% of the detected genes confirmed differential clustering of the three groups (Fig. 8b). The most notable separation among these groups was evident along the PCA2 axis, representing only 12.3% of the genes. It was along this axis that the LCMV-infected CVI mice separated more distinctly from the other two groups.

We next used Ingenuity Pathway Analysis (IPA) to delve more deeply into the concordant dysregulated gene expression in uninfected vs. previously infected mice at day 20 post-CVI relative uninjured controls (Fig. 8c,d; Supplementary Tables 2–4). Following CVI, uninfected mice expressed genes associated with acute phase response signaling (p = 1.26e-16), granulocyte adhesion and diapedesis (p = 1.58e-15), and neuroinflammation signaling (p = 7.94e-14), among other pathways (Fig. 8c; Supplementary Table 2). By contrast, CVI mice that were previously infected with LCMV on day 4 showed a different gene expression signature in the neocortex on day 20. Upregulated genes were associated with interferon signaling (p = 3.16e-14), acute phase response signaling (p = 1.58e-11), and the complement system (p = 3.98e-11) when compared to uninjured controls (Fig. 8d; Supplementary Table 3). Among canonical interferon pathway genes, 19% were upregulated in uninfected CVI mice (p = 1.41e-07) relative to 36% in the LCMV-infected group (p = 3.16e-14) (Fig. 8e,f; Supplementary Table 4). Top transcriptional regulators including *STAT1* (Z-score = 5.031), *STAT2* (Z-score = 2.24), *IRF7* (Z-score = 6.738), and *IRF9* (Z-score = 2.088) were activated by prior infection. Comparison of a more extensive list of genes directly or indirectly linked to interferons revealed substantial dysregulation in the neocortex of day 4 infected CVI mice relative to uninfected (Fig. 8g; Supplementary Table 4). These results demonstrate that systemic infection following CVI leads to long term activation of the IFN-I pathway.

To determine the impact of this differential programming on functional recovery, we evaluated cognitive-motor function by Y-maze in uninjured control mice as well as uninfected and day 4 LCMV-infected CVI mice at day 20. We demonstrated previously that CVI mice (relative to uninjured controls) lose cognitive-motor function as assessed by Y-maze at day 10, which is followed by functional recovery at day 20[27]. We confirmed this result by showing that uninfected CVI mice at day 20 performed similarly to uninjured controls in the Y-maze test (Fig. 8h,i). By contrast, LCMV-infected mice did not recover function at day 20 post-CVI, demonstrating a sizeable reduction relative to their uninfected counterparts (Fig. 8h,i). To determine if IFN-I signaling impeded functional recovery in infected mice, we also evaluated Y-maze performance in IFNAR$^{-/-}$ CVI mice that were either uninfected or infected at day 4 with LCMV. Importantly, infected IFNAR$^{-/-}$ mice demonstrated improved functional recovery relative to infected B6 controls (Fig. 8h,i). The functional recovery in IFNAR$^{-/-}$ mice consisted of a partial improvement in the number of gates entered (Fig. 8h) as well as a complete recovery of triplicate ratio performance (Fig. 8i). Collectively, these data indicate that systemic infection interferes with recovery of neurological function after CVI via a mechanism that depends in part on IFN-I signaling.

Discussion

Our study provides important insights into how systemic infections interfere with the recovery process after brain injury. We demonstrate that a broad range of infections and PAMPs disrupt vascular repair following TBI and CVI. In fact, sequential infections encountered after mTBI induce a chronic state of disrepair. At least one mechanism by which infectious agents disrupt repair is via IFN-I induction. These cytokines deviate reparative programming in myeloid cells and alter their spatial distribution in damaged CNS tissue. This disruptive process is induced by the innate viral sensor, MDA-5, after LCMV infection. However, it is expected that other innate sensors triggered by different pathogen types will have a similar negative impact on CNS repair. It is nevertheless clear that one disruptive thread common to many infections is IFN-I production, which we show interferes with both meningeal and parenchymal vascular remodeling. Especially devastating is the effect of infection on CVI – a scenario that not only impedes angiogenesis but also promotes chronic IFN-I signaling, downregulation of tight junction proteins, BBB leakage, and a failure to recover neurological function.

Our data show that different classes of infectious agents and PAMPs encountered after mTBI impede meningeal vascular repair[26]. Previous rodent studies demonstrated that systemic LPS administration one month following TBI induces CNS inflammation that leads to progressive cognitive decline[38,39]. Streptococcal pneumonia in mice also promoted poor motor recovery and mortality after TBI[40]. In the periphery, wound healing is severely inhibited by bacteremia, sepsis, or distal inflammation[17,18], which is attributed to dysregulation of the early innate immune response crucial for wound healing[23,41]. Approximately 20–50% of patients hospitalized with TBI have some type of infection[7,9]. These infections are associated with poor acute- and long-term outcomes[12–14]. Multiple infections are also common in patients with moderate-severe TBI due to post-injury immunosuppression[42] as well as an increased frequency of sepsis that renders the host susceptible to opportunistic secondary infections[43]. The association between sepsis and mortality in TBI patients extends up to 1 year after injury[12], and pneumonia is independently associated with poor outcomes in severe TBI patients, extending out to 5 years post-injury[13]. Based on our findings, it is important to consider aggressive approaches to prevent and/or treat infections following brain injury.

While many different inflammatory mediators are generated in response to infection, we show that IFN-I is the major disruptor of repair in injured mice challenged with LCMV, LPS, or *C. albicans*. All known IFN-I's were detected in LCMV-infected mTBI mice, and knock out or inhibition of IFNAR restored meningeal vascular repair. Moreover, transcranial IFN-β1 administration (without infection) alone was able to impede meningeal repair. It is well known that IFN-I's orchestrate innate and adaptive immunity against viruses[34,44]; however, bacteria, parasites, and fungi can also elicit IFN-I responses[45]. IFN-I is produced after pathogens are recognized by many different PAMP receptors[46]. For example, LCMV is detected by retinoic acid-inducible gene I and MDA5 (two cytosolic pathogen recognition receptors)[35]. We observed reduced IFN-I expression and normal meningeal repair in MDA5$^{-/-}$ mice, suggesting that the detection and response to viral infection is what inhibits repair after mTBI. Brain injury even without infection can elicit some detrimental IFN-I production. Rodent studies demonstrated that release of cytosolic and mitochondrial nucleic acids by injured cells activates the cGAS-STING pathway, resulting in IFN-I production[47]. This IFN-I enhances secondary neuroinflammation and neurodegeneration[48,49]. We observed that viral infection elevates expression of IFN-I after mTBI, which likely amplifies the already deleterious effects of these cytokines[47–49].

Myelomonocytic cells play a central role in orchestrating repair after injury[23]. While the acute response to infection bears similarities to wound-healing responses[50,51], distal viral infections can nevertheless dampen the innate inflammatory response to peripheral wounds, which delays healing[52,53]. Meningeal repair following mTBI requires a precise arrangement of different macrophage subsets in the lesion core and perimeter to scavenge dead cells and promote angiogenesis, respectively[26]. Our studies demonstrate that viral infection fundamentally alters this spatial distribution of myeloid cells. IFNAR signaling causes pro-inflammatory myelomonocytic cells to decrease in the mTBI lesion core after infection and redistribute to the lesion perimeter where they comingle with wound-healing macrophages. Transcranial administration of IFN-β1 to a mTBI lesion promoted myeloid cell recruitment within hours, and deletion of IFNAR specifically from LysM^{+} myelomonocytic cells completely restored meningeal repair. In addition, deletion of MDA5 eliminated the ISG response to LCMV while allowing upregulation of myeloid cell-recruiting chemokines like CCL2 and CCL4 in response to injury. These data demonstrate that a single signaling pathway (IFNAR) is responsible for redirection of the CNS immune-mediated wound-healing program.

We also observed faulty repair in the brain parenchyma following systemic LCMV infection of mice with ultrasound-induced CVI (a model of hemorrhagic stroke). One third of all acute stroke hospitalizations are complicated by systemic infections, which are linked to poor outcomes both short- and long-term[6,8]. Infections may also increase the risk of recurrent stroke[54]. Prophylactic antibiotics have failed to prevent infection rates or affect associated outcomes, due to stroke-induced systemic immunosuppression[10,16]. In rodent studies of ischemic stroke, acute LPS administration exacerbated brain damage and neurological deficit via IL-1-induced potentiation of neutrophil mobilization[55]. While the immunology and vasculature of the meninges and brain parenchyma are different[21], our data indicate that infection-induced IFN-I impedes reparative angiogenesis similarly in both compartments. Angiogenesis is critical for repair of injured brain tissue[56], and vascular density is associated with improved outcomes following CVI[57]. Circulating inflammatory monocytes were shown to help mature neo-vessels[36] and promote functional recovery[37] following stroke. Specific deletion of IFNAR from LysM$^+$ myelomonocytic cells resulted in complete restoration of meningeal vascular repair following mTBI, but only a partial improvement in parenchymal repair after CVI. This finding is likely due to the detrimental effects that IFN-I has on other parenchymal residents, such as microglia, astrocytes and pericytes[28].

Systemic viral infection after CVI not only impeded angiogenesis but also led to chronic IFN-I signaling, decreased tight junction proteins, persistent BBB leakage, gliosis, neuronal loss, and a failure to recover neurological function. Importantly, genetic deletion of IFNAR markedly improved functional recovery in virally infected CVI mice. Cerebrovascular disease has been associated with an increased risk of developing neurodegenerative dementia[4,58], and imaging studies suggest that cerebral ischemia may initiate a long-term neurodegenerative process[59,60]. One-third of stroke patients have cognitive impairment within the first months following their ischemic event[61]. Persistent BBB leak is a possible driver of dementia in the setting of cerebrovascular disease[62], and systemic inflammatory markers in stroke survivors are associated with progressive degeneration[63,64]. In rodents, LPS administration during reperfusion of mice that underwent middle cerebral artery occlusion increased brain atrophy one-month post-injury[65]. Based on our data in CVI mice, we postulate that acute infections following CVI in humans can induce a chronic state of disrepair, BBB leakage, and inflammation, leading to neurodegeneration.

In conclusion, our study provides fundamental insights into how systemic infections impede recovery following TBI and CVI. CNS tissue repair requires a spatially, temporally, and functionally coordinated innate immune response[26,27]. Single or recurrent infections encountered during the recovery period can deviate or halt this reparative response. In TBI and CVI patients, infections are common and result in poor outcomes, but treatment options are not currently available[6–9]. We believe that new therapeutic opportunities exist to improve outcomes in TBI and CVI patients via modulation of antimicrobial immunity and that a search for associated pathogens should be initiated in patients experiencing a chronic state of disrepair following CNS injury.

Methods

Mice.

C57BL/6J (B6), B6.129P2-Lyz2tm1(cre)Ifo/J (LysMCre/Cre)[66], loxP-flanked *Ifnar1* (B6(Cg)-Ifnar1tm1.1Ees/J; IFNAR$^{fl/fl}$)[67], B6.Cg-Ifih1tm1.1Cln/J (MDA5$^{-/-}$)[68], B6.129P-CX3CR1tm1Litt/J (CX3CR1$^{gfp/gfp}$)[69], and B6.129(Cg)-Ccr2tm2.1Ifc/J (CCR2$^{rfp/rfp}$)[70] mice were purchased from Jackson Laboratories and were then bred and maintained under specific pathogen-free conditions at the National Institute of Health (NIH). Type I interferon-α/β receptor 1-deficient mice on B6 background (IFNAR$^{-/-}$)[71] were provided by Jonathan Sprent (Scripps Research Institute, La Jolla, CA) and then bred and maintained under specific pathogen-free conditions at the National Institute of Health. LysMCre-IFNAR$^{fl/fl}$ mice were obtained in the F2 generation by originally crossing LysM$^{Cre/Cre}$ and IFNAR$^{fl/fl}$ mice and were screened using PCR. CX3CR1$^{gfp/wt}$ CCR2$^{rfp/wt}$ double reporter mice were generated from an F1 cross of CX3CR1$^{gfp/gfp}$ and CCR2$^{rfp/rfp}$ mice. All mice in this study were handled in accordance with the guidelines set forth by the NIH Animal Care and Use Committee and the recommendations in the AAALAC Guide for the Care and Use of Laboratory Animals. The protocol was approved by the NINDS Animal Care and Use Committee. Male and female mice in this study were used at 8–12 weeks of age with age matched control groups. Mice were bred and maintained under specific pathogen-free conditions at the National Institute of Health. Housing conditions included temperature 72 F, humidity 50% and light/dark cycle 12h each.

Mouse surgeries were based on adapted techniques previously developed in our laboratory[72]. For the experiments, 8- to 12-week old mice (weighing 24–28 g) were anesthetized with ketamine (85 mg/kg), xylazine (13 mg/kg) and acepromazine (2 mg/kg) in PBS and maintained at core temperature of 37°C. An incision over the midline of the scalp was planned, the hair was removed using clippers, and lidocaine was applied to the scalp, which was then cleaned using ethanol. Subsequently, an incision was completed to expose the skull and the periosteum was removed using a microsurgical blade. After the specific procedure was competed (described below), the incision was closed with wound clips, and mice were injected subcutaneously with 0.1 mg/kg Buprenex for pain management. Mice were kept warm until they fully recovered from anesthesia.

Mild traumatic brain injury model.

All TBI experiments were performed as previously described [25,26,72]. Following surgical exposure of the skull bone (described above), a metal bracket was secured on the skull bone over the right barrel cortex (2.5 mm from bregma × 2.5 mm from the sagittal suture). A square cranial window (1 mm × 1 mm) was thinned to a thickness of ~20 μm within 30–60 sec. The blunt end of a microsurgical blade was used to lightly compress the skull bone 10 times into a concavity without cracking the skull.

Cerebrovascular injury (ultrasound) model.

All cerebrovascular injury (CVI) experiments were performed as previously described[27]. Following surgical exposure of the skull bone (described above), a metal bracket was glued to the skull leaving exposed a circular area of bone centered 2 mm posterior to Bregma and 2.5 mm from the sagittal suture. A 2 × 2 mm cranial window was carefully thinned to 20–25 μm within 10–15 min. A suspension of Perflutren protein-Type A microspheres (5 to 8×10^8 bubbles/ml with a size range of 2.0 to 4.5 μm.; Optison™, GE Healthcare) was injected intravenously (i.v.) via the retroorbital route at a dose of 1 μl per g of mouse weight. Subsequently, a drop of CSF was placed over the cranial window. We then applied low intensity pulse ultrasound (LIPUS) at 1MHz with peak negative pressure ~ 200KPa (2.2 W/cm2), 1 ms burst length, 10% duty cycle, and 10 sec exposure to the thinned skull using a Sonicator 740x (Mettler Electronics) with a 5 cm^2 dual frequency applicator.

Infections, PAMPs, and cytokine administration.

Acute LCMV infection was initiated by i.v. administration of LCMV Armstrong clone 53b (2×10^6 plaque forming units or PFU) at day 4 and/or day 10 post-mTBI or CVI. A colony of persistently infected LCMV carrier mice was initially generated by infecting 1-day-old B6 mice intracerebrally with 10^3 PFU of LCMV Armstrong as described previously[73]. The resultant mice were then bred to maintain the persistently infected colony (LCMV carrier mice). VSV Indiana was administered intranasally at a dose of 1×10^5 PFU per nostril (total dose 2×10^5 PFU) 1 day prior to mTBI or 10 days after mTBI. Viral stocks were prepared by a single passage on BHK-21 cells, and viral titers were determined by plaque formation on Vero cells[74]. Fungal infections were initiated by i.v. injection of 1×10^5 cells of *Candida albicans* strain SC5314 on day 3 following mTBI. A single colony grown 48 hours at 37°C on yeast extract peptone dextrose (YPD) agar plates was used to inoculate YPD broth containing penicillin and streptomycin (Mediatech). Yeast was grown at 30°C in a shaking incubator and serially passaged three times, with growth periods ranging from 18–24 hours at each passage. Upon final passage, yeast cells were harvested by centrifugation at 1400 rpm for 7 minutes and washed twice with sterile PBS. A hemocytometer was used to count yeast cells and create a suspension of 1×10^5 cells to 100 μl in PBS[75]. Polyinosinic-polycytidylic acid (poly(I:C); Invivogen) was administered i.v. at a dose of 200 μg 4 days following mTBI. *Lipopolysaccharides* from *Escherichia coli* O55:B5 (LPS; Sigma Aldrich) were administered i.v. at a dose of 10 μg 4 days following mTBI. IFNβ1 (PBL assay science) was administered i.v. on days 5 and 6 post-mTBI (2×10^5 units per injection). IFNβ1 was also administered transcranially through a thinned skull bone as described previously[25]. On days 5 and 6 following the initial mTBI, the original incision was re-accessed, and a metal bracket was glued on the skull leaving exposed a circular area of the skull centered over the TBI window. IFNβ1 was diluted in artificial cerebral spinal fluid (aCSF; Harvard Apparatus) at a concentration of 10^4 units per ml, and 200 μl was applied directly to the skull bone as a 3 mm diameter bubble for 6 hours. For the control group, aCSF was applied. The solution was replenished as needed over the 6-hour period to prevent drying. A total of 0.5–1 ml of solution was used per animal per day. Transcranial IFNβ1 was administered in mice following unilateral mTBI as well as bilateral mTBI. For the bilateral mTBI paradigm, IFNβ1 was applied to one injury and aCSF to the other in the same mouse.

Antibody treatment.

To block IFNAR, we administered a single dose of 500 μg αIFNAR antibody (MAR1–5A3; BioXcell) in PBS i.p. on day 3 after mTBI or CVI, 1 day prior to LCMV, LPS or *Candida albicans* administration. Animals were evaluated on day 7 after mTBI or day 10 after CVI.

Immunohistochemistry.

Meninges were harvested on days 1, 3, 5, and 7 post-mTBI injury. Vasculature was labeled by i.v. injection of 70 μl DyLight 649 labeled Lycopersicon Esculentum (Tomato) Lectin (Vector Labs) 5–10 min before euthanasia. A 5 × 5 mm area of skull including the mTBI injured meninges was carefully dissected with scissors and placed in PBS containing Background Buster (Innovex Biosciences,) as well as 1:500 purified rat anti-mouse CD16/CD32 (Fc receptor block; clone 93, BioLegend) (blocking buffer) for 30 min at room temperature (20–25 °C). Primary antibodies were added directly to the blocking buffer and incubated at 4°C overnight. After primary staining, slices were washed three times in staining buffer (PBS containing 2% fetal bovine serum). Secondary antibodies were added and incubated for 4 h at room temperature (20–25 °C). Meninges were again washed three times in staining buffer and placed in 4% paraformaldehyde overnight. Meninges were removed from the skull by careful peeling using fine-tipped forceps. The free-floating meninges were placed flat in one drop of FluorSave Reagent (MilliporeSigma) on a slide and a coverslip was added. The meninges were stained with the following primary antibodies: anti-CD11b Pacific blue (1:300; M1/70; BioLegend), anti-CD206 AlexaFluor 488 (1:500; C068C2; BioLegend), polyclonal anti-laminin (1:500; catalog# ab11575; Abcam). The following secondary antibody was used: rhodamine red-X conjugated donkey anti-rabbit (1:1000; Jackson ImmunoResearch).

Brains were harvested 10 days post-injury. For vascular staining, mice were injected i.v. with 70 μl fluorescence-conjugated tomato lectin Dylight 649 or fluorescence-conjugated tomato lectin Dylight 488 (Vector Labs) 5–10 min prior to euthanasia. To evaluate blood brain barrier (BBB) leakage, mice were injected with 100 μl of 0.1 mg/ml Evans blue (Sigma) i.v. one hour prior to euthanasia. Mice then received an intracardiac perfusion with 4% paraformaldehyde. Afterward, brains were harvested and placed in 4% paraformaldehyde overnight. Fixed brains were sectioned axially or coronally using a Compresstome Tissue Slicer (Precisionary). For staining, tissues were initially blocked and permeabilized by incubating with PBS containing 0.5% Triton-X, Background Buster (Innovex biosciences), and FcR block (blocking buffer) for 30 min at room temperature (20–25 °C). Primary antibodies were added directly to the blocking buffer and incubated at 4°C overnight. After primary staining, slices were washed three times in staining buffer (PBS containing 2% fetal bovine serum). Secondary antibodies were added and incubated for 4 h at room temperature (20–25 °C). After secondary staining, slices were washed again three times in staining buffer. The free-floating slices were carefully mounted on the slide and covered with one drop of FluorSave Reagent (MilliporeSigma) and a coverslip was added. The tissues were stained with the following primary antibodies: rabbit anti-Iba1 (1:500; catalog# 019–19741; Wako), chicken anti-GFAP (1:1000; catalog# ab4674; Abcam), guinea pig polyclonal anti-NeuN (1:500; catalog# ABN09P; Millipore), rabbit anti-claudin-5 (1:250; catalog# 341600; ThermoFisher), rabbit anti-ZO-1 (1:250; catalog# ab96587) conjugated to Alexa fluor 647 using antibody labeling kit (Invitrogen). Secondary antibodies (1:1000 dilution) included: donkey anti-rabbit IgG (H+L) Alexa Fluor 488 (1:1000; A-21206; ThermoFisher), donkey anti-rabbit IgG (H+L) Alexa Fluor 594 (A-21207; ThermoFisher), goat anti-guinea pig IgG (H+L) Alexa Fluor 647 (A-21450; ThermoFisher), and donkey anti-chicken IgY (IgG) (H+L) DyLight 405 (AB_2340373; Jackson Immunoresearch).

Confocal imaging and analysis.

Confocal images were obtained using an Olympus FV1200 laser-scanning confocal microscope equipped with four detectors, six laser lines (405, 458, 488, 515, 559 and 635 nm) and five objectives (4 × /0.16 NA, 10 × /0.4 NA, 20 × /0.75 NA and 40 × /0.95 NA, and chromatic aberration–corrected 60 × /1.4 NA). For imaging acquisition, the Leica Application Suite X (LAS X) 3.5.5.19976 was used. All confocal images were subsequently imported into Imaris version 9.3 software (Bitplane Inc.) for additional analyses performed by a blinded investigator. mTBI lesions were quantified in meningeal tissue harvested 7 days after mTBI injury in uninfected vs. LCMV-infected B6, IFNAR$^{-/-}$, LysMCre-IFNAR$^{fl/fl}$ and MDA5$^{-/-}$ mice. Lesions were also quantified 7 days after injury in mice treated with i.v. LPS, i.v. polyI:C, i.v. or transcranial IFNβ1 as well as LCMV infected vs. uninfected mice treated with αIFNAR antibody. The meninges of uninfected B6 mice were also evaluated 1, 3, 5, and 7 days post-mTBI injury. To quantify meningeal vasculature, we used the surfaces function in Imaris as described previously[26]. At different time points post-injury, the entire meningeal lesion induced by mTBI (both repaired and non-repaired) was identified and circumscribed using Imaris. The total lesion area was identified based on regions containing small laminin-positive, Tomato lectin-positive neo-vascular loops (i.e., repaired vasculature) as well as those containing laminin-positive, Tomato lectin-negative vessels (i.e., unrepaired / damaged blood vessels)[26]. The area of unrepaired meninges was also determined, and the final percentage of repaired meningeal tissue was calculated using the following equation:

$$\%\ \text{repair} = \frac{\text{Total lesion area} - \text{unrepaired area}}{\text{Total lesion area}} \text{ x } 100$$

Cell number quantification was completed using meningeal samples harvested 5 days post-mTBI from uninfected and LCMV-infected mice. We generated ‘spots’ in Imaris for all immunohistochemically labeled CD11b^{+} and CD206^{+} cells within the lesion core as well as within the peri-lesion area. For this quantification, a 1.5 mm × 1.5 mm region of interest was centered on the middle of the lesion. We next identified CD11b^{+}CD206^{+} cells using the ‘spots’ colocalization function. We then calculated the total number of individual CD11b^{+} cells as well as the number of CD11b^{+}CD206^{+} and CD11b^{+}CD206^{-} cells in the lesion core and peri-lesion area.

To quantify BBB leakage, mice were injected with 100 μl of 0.1 mg/ml Evans blue (Sigma) i.v. 10 days after injury and 1 h prior to euthanasia as described above. Following processing and confocal imaging of the brain slices, images were imported into Imaris version 9.3 software. For quantification of Evans blue extravasation and GFAP+ gliosis, a 100 μm axial section encompassing the entire surface of the CVI-damaged hemisphere was cut and a 4x confocal tile scan was acquired. The resultant tile scans were imported into Imaris and a ‘surface’ corresponding to Evans blue or GFAP signal was generated and used calculate sum fluorescence intensities. Control axial brain hemispheres stained only with secondary antibody was used to determine the background signal and set the absolute intensity thresholds to create ‘surfaces’ for Evans blue and GFAP signal. We also quantified the number of NeuN^+ neurons and Iba1^+ microglia / macrophages in similar axial brain slices harvested 10 days after injury using the ‘spots’ function in Imaris and divided by the three dimensional volume of the acquired image to obtain the cell density (i.e., number of cells per mm^3).

For tight junction analysis, areas of injury were identified in coronal mouse brain sections from uninfected and d4 LCMV-infected B6 mice at day 20 post-CVI. For vascular staining, mice were injected i.v. with fluorescence-conjugated tomato lectin Dylight 488 (Vector Labs) 5–10 min prior to euthanasia. Sections were subsequently stained with antibodies against claudin-5 and ZO-1. After processing and confocal imaging of the brain slices, images were imported into Imaris version 9.3 software. Using Imaris, ‘contours’ were generated around all individual blood vessels in each mouse brain section based on tomato lectin Dylight 488 signal and used to create a 3D surface. The total volume of this surface was calculated using the ‘statistics’ function (vascular volume). Afterward, the claudin-5 and ZO-1 sum fluorescence intensities (total # voxels x mean fluorescence intensity) within this surface were measured using the ‘statistics’ function and the intensity per unit area was calculated as follows:

$$\text{Fluorescence intensity per vascular volume} = \frac{\text{Sum fluorescence intensity}}{\text{Vascular volume}}$$

Intravital two-photon imagine and analysis.

Ten days following CVI, the original incision was re-accessed and a metal bracket was glued onto the skull leaving exposed a circular area of the skull that was thinned previously to 20–25 μm. Images were obtained using a Leica SP8 two-photon microscope with an 8,000-Hz resonant scanner, a 25 × collar-corrected water-dipping objective (1.0 NA) or a 20 × water-dipping objective (1.0 NA), a quad HyD external detector array, a Mai Tai HP DeepSee Laser (Spectra-Physics) tuned to 905 nm (for GFP, Dylight 488, and RFP) and an Insight DS laser (Spectra-Physics) tuned to 1,050 nm (for Evans blue). For image acquisition the Leica Application Suite X (LAS X) 3.5.5.19976 was used.

For evaluation of angiogenesis and characterization of neo-vessels, mice were imaged 10 days post-CVI. To visualize blood vessels mice were injected i.v. with 70 μl of 0.1 mg/ml Evans blue (Sigma) and/or 70 μl tomato lectin Dylight 488 (Vector Labs) prior to imaging. Three-dimensional (3D) z-stacks (100–120 μm depth) were captured using a 3-μm step size. The signal contrast was enhanced by averaging 8–10 frames per plane in resonance scanning mode. The 3D z-stacks were then imported to Imaris 9.3. The volume of vascular coverage was quantified using the ‘surfaces’ function for Evans blue and tomato lectin signal. We subsequently masked the areas negative for Evans blue and tomato lectin also using the ‘surfaces’ function. We identified all intervascular spaces and calculated the average intervascular area. This methodology was used to evaluate angiogenesis in uninfected B6 mice 10 days following CVI as well as LCMV infected B6, IFNAR$^{-/-}$, LysMCre-IFNAR$^{fl/fl}$, MDA5$^{-/-}$, and αIFNAR treated B6. All image analysis was performed by a blinded investigator. To evaluate the effect of IFNβ1 on myeloid cell distribution following mTBI, CX3CR1$^{gfp/wt}$ CCR2$^{rfp/wt}$ mice were evaluated at day 5. Three-dimensional time-lapses of the injured meninges were obtained before transcranial IFNβ1 administration as well as for 2 to 3 hrs following administration. To generate time lapses, 100 μm *z*-stacks (3-μm step size) were captured at a 5 min time interval. Signal contrast was enhanced by averaging 6 frames per plane in resonance scanning mode. Time lapses were then imported into Imaris 9.0, and CCR2$^+$ cells were subsequently manually counted at 90 min following transcranial incubation with IFNβ1. At the 90 min time point, CCR2$^+$ monocytes were identified as 20–30 μm RFP+ cells whose movement could be followed over at least 3 frames. Videos were processed using Adope Premiere Pro 14.0.

BBB integrity assay.

BBB integrity was assessed at 1h, 1d, 3d, 5d, 7d, 10d and 20d post-CVI. At the denoted time points, we administered 1 mg of sodium-fluorescein (Na-fl; 100 μl of 1% w/v Na-fl in PBS; Sigma) i.v. 10 min prior to euthanasia. Mice were perfused with PBS prior to harvesting the injured hemisphere. Tissues were homogenized in 1 ml of 7.5% trichloroacetic acid (TCA) and centrifuged at 10,000 g at 4°C. Following centrifugation, supernatants were collected and 200μl of 5N NaOH was added. Fluorescence was quantified using a fluorometer (Varioskan Flash; ThermoFisher) at an excitation at 485 nm, emission at 530 nm and a gain of 50. We generated a standard curve by plotting mean fluorescence intensity (MFI) versus Na-fl concentration (mg/ml) for known standards (ranging from 2×10^{-6} to 8×10^{-3} mg/ml) diluted in brain tissue lysate. This standard curve was used to calculate the concentration of Na-fl in our samples. The total amount of Na-fl in each sample was expressed as a percentage of the initial injected dose (1 mg).

Real-time PCR analysis.

mTBI and control mice received an intracardiac perfusion with saline. Afterward, 2 × 2 × 2 mm cube of superficial cortical tissue and meninges was removed. This included the mTBI lesion as well as some surrounding brain tissue. The tissue was snap frozen using dry ice. Total RNA was extracted with a Qiagen Micro RNA kit (Qiagen) following the manufacturer’s protocol. RNA quantity and integrity were assessed using a spectrophotometer (Nanodrop One, Thermoscientific). cDNA was generated using an iScript cDNA Synthesis kit (Bio-Rad). Pre-made commercial and custom made PrimePCR plates were used for qPCR experiments (Angiogenesis M96, Type I interferon response M96, type I interferon custom-made plate; Bio-Rad) (see Supplementary Table 1 for individual genes). qPCR was performed using universal SYBR Green Supermix (Bio-Rad) and cDNA template or water (non-template negative control) at an annealing temperature of 60°C with a CFX96 Real-Time PCR machine (Bio-Rad). PCR products were subjected to melt analysis to confirm purity after DNA amplification. For each gene, expression values were normalized to the *Gapdh* housekeeping gene. The resulting relative gene expression was then expressed as a fold-change from uninjured control samples (δδCT).

Bulk RNA sequencing.

For RNA sequencing, B6 mice were divided into 3 groups, uninjured (Ctrl), injured (CVI), injured and LCMV-infected (CVI LCMV) with 4 mice per group. At day 20 following CVI, mice were perfused with normal saline, and a 3 × 3 × 3 mm cube of injured tissue was harvested and snap frozen using dry ice. Total RNA was extracted with a Qiagen Micro RNA kit following the manufacturer’s protocol. RNA quantity and integrity were assessed using a Bioanalyzer (Agilent). 500 ng of total RNA was used in conjunction with the TruSeq® Stranded Total RNA Library Prep kit (Illumina). Library quality was checked with a Bioanalyzer and quantified by Qubit (ThermoFisher Scientific). Equimolar quantities from each sample library was pooled and run on a Highoutput Next-Seq550 kit (Illumina). Sequencer output files were deposited in the NCBI Short Read Archive via the Gene Expression Omnibus submission process (https://www.ncbi.nlm.nih.gov/geo/query/acc.cgi?acc=GSE172102).

RNA sequencing data analysis.

Paired-end sequence files (.fastq) per sample were quality inspected using the FastQC tool 0.11.8 (https://www.bioinformatics.babraham.ac.uk/projects/fastqc/) then adaptor clipped (TruSeq3-PE-2.fa:2:30:10) and trimmed to remove 5’ nucleotide bias (HEADCROP:11) and low quality calls (TRAILING:20 SLIDINGWINDOW:4:20 MINLEN:15) using the Trimmomatic tool 0.39 (http://www.usadellab.org/cms/?page=trimmomatic). Surviving intact pairs of reads per sample were then imported into the CLCbio Genomics Workbench v11 (https://www.qiagenbioinformatics.com/), down-sampled to 40M read pairs per sample, then reference mapped by sample in stranded fashion against the current instance of the mouse genome (GRCm38) using the “RNA-Seq Analysis” tool supported therein under default parameters. Expression per known annotated gene (Mus_musculus.GRCm38.83.chr.gtf) in Transcripts Per Kilobase Million (TPM) units was then exported from the Workbench and imported into R (https://cran.r-project.org/). In R (v3.6.2), TPM expression per sample was pedestalled by 2 then Log2 transformed. Genes lacking an expression value >1 post transformation for at least one sample were discarded while expression across samples for genes not discarded were quantile normalized. To assure quality of the data post normalization and absence of sample-level outliers, exploratory inspection was performed using Tukey box plot, covariance-based PCA scatterplot and correlation-based heat map. To remove noise-biased expression values, locally weighted scatterplot smoothing (LOWESS) was applied across normalized expression for all genes by sample class (Coefficient of Variation~mean expression). LOWESS fits were then over-plotted and inspected to identify the common low-end expression value where the relationship between mean expression (i.e., “signal”) and Coefficient of Variation (i.e., “noise”) grossly deviated from linearity. Expression values were then floored to equal this value if less, while expression for genes not observed greater than this value for at least one sample were discarded as noise-biased. For genes not discarded, expression differences across sample classes were tested for using the one-factor Analysis of Variance (ANOVA) test under Benjamini–Hochberg (BH) False Discovery Rate (FDR) Multiple Comparison Correction (MCC) condition using sample class as the factor. Genes having a Type III corrected $P < 0.05$ by this test were then subset and the TukeyHSD post-hoc test used to generate mean differences and p-values for each possible pairwise comparison of classes.

Genes having a post-hoc $P < 0.05$ for a specific comparison and a linear difference of means >= 1.5× for the same comparison were deemed to have expression significantly different between the compared groups. Post testing, sample-to-sample relationships were investigated via covariance-based PCA scatterplot and Pearson correlation-based clustered heat map using the unique union of genes deemed to have a significant difference of expression between at least two classes. Enriched pathways, functions, and top scoring networks for the same union set of genes were obtained using the Ingenuity Pathway Analysis (IPA) tool (https://www.qiagenbioinformatics.com/).

Cognitive-motor function test.

The cognitive-motor function of B6 mice following sham surgery as well as injured B6 and IFNAR$^{-/-}$ mice with or without LCMV infection was evaluated at day 20 post-injury using a Y-maze with three white, opaque plastic arms at 120° angles from one another. Mice were placed in the center of the maze and allowed to freely explore for 5 min per session. An entry was defined when all four limbs were within the arm. We recorded the total number of arm entries to assess the overall movement in the maze. We also recorded the number of times the mouse sequentially entered all 3 arms (e.g. $A \rightarrow B \rightarrow C$ not $A \rightarrow B \rightarrow A$) as a measure of exploration and cognitive function. The number of triplicate $A \rightarrow B \rightarrow C$ entries was divided by total number of gates entered to obtain the “triplicate ratio”. Each mouse was evaluated at one time point.

Statistical analysis.

Statistical analysis and graph design were performed using Prism 8.4 (GraphPad Software) except for bulk RNA sequencing analysis, which we describe in detail above. Distribution normality was assessed using the Shapiro-Wilk normality test. Experiments containing two groups were analyzed using a two-tailed Student’s t-test for normally distributed data or the Mann–Whitney U test for non-normally distributed data. Experiments involving more than two groups were analyzed by One-Way ANOVA followed by Tukey multiple comparison’s test for normally distributed data or Kruskal-Wallis test followed by Dunn’s multiple comparison’s test for non-normally distributed tests. Data grouped based on more than one nominal variable were analyzed using a Two-way ANOVA followed by the Holm-Šídák multiple comparison method. Groups were considered statistically different at $P < 0.05$. All data are displayed as the mean ± standard deviation (SD). For the qPCR data analysis, we used two-way ANOVA followed by the Holm-Šídák multiple comparison method or multiple t-tests using the Benjamini, Krieger and Yekutieli method, to correct for the false discovery rate, with a desired Q value of 1% or 5%. Statistical analyses for each graph are provided in Supplementary Table 5. No statistical methods were used to predetermine sample sizes, but our sample sizes are similar to those reported in previous publications[25–27]. Animal littermates were randomly assigned to each group, and samples were randomly selected for data acquisition and analysis; no active randomization protocol was used.

Ethics statement.

This study was carried out in strict accordance with the recommendations in the Guide for the Care and Use of Laboratory Animals of the National Institutes of Health. The protocol was approved by the NINDS Animal Care and Use Committee (Protocol Number: 1295–20).

Accession codes.

Our bulk RNA-seq data are available in the NCBI Gene Expression Omnibus under access code GSE172102.

Data Availability.

The data that support the findings of this study are available from the corresponding author upon request. There are no restrictions on data availability. Bulk RNA-seq data are available in the NCBI Gene Expression Omnibus under accession code GSE172102. The mouse genome database used in our RNA sequencing analysis was GRCm38 (https://www.ncbi.nlm.nih.gov/assembly/GCF_000001635.20/). Each figure has associated source data provided in the supplementary section of this manuscript.

Extended Data

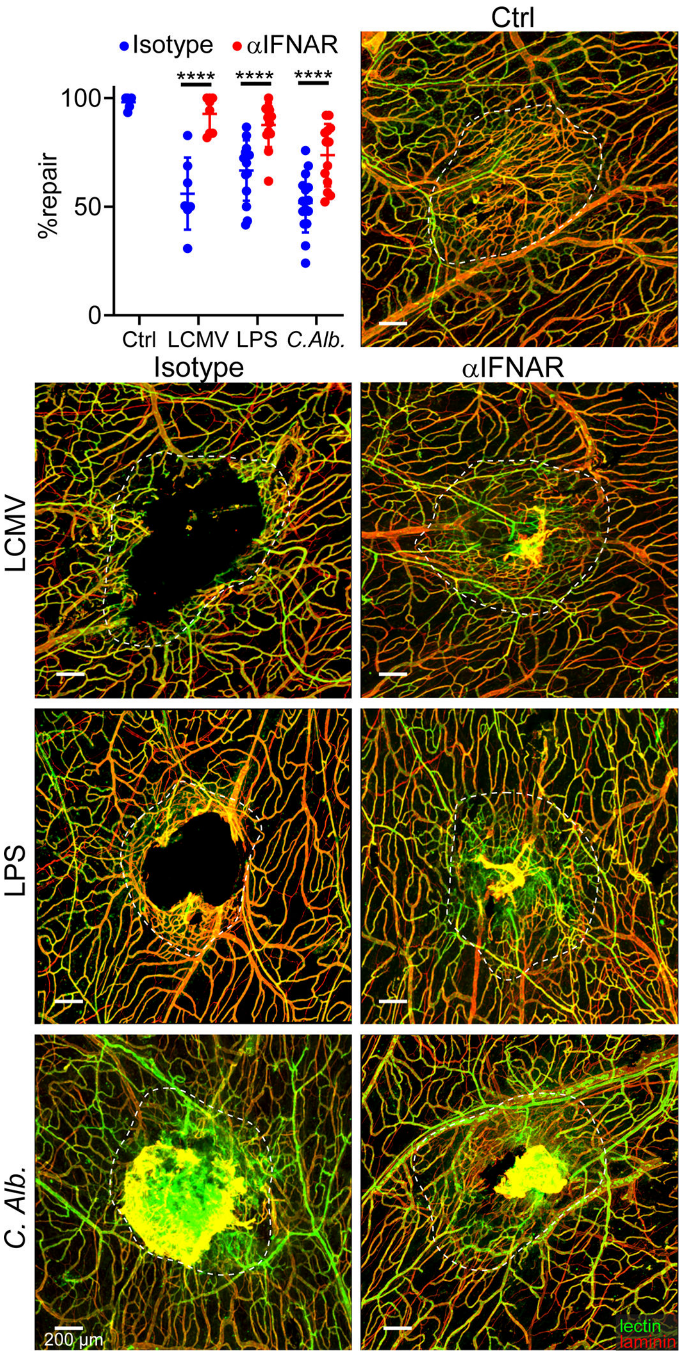

Extended Data Fig. 1. Inhibition of interferon signaling improves meningeal repair after mTBI.

The dot plot depicts the percent of meningeal lesion repair 7 days after mTBI in uninfected mice (Ctrl) as well as mice challenged with LCMV, LPS, or Candida albicans (C. Alb) on day 4 post-injury, with or without αIFNAR antibody treatment. Cumulative data from two independent experiments. Each symbol represents an individual mouse, and asterisks denote statistical significance. Data are represented as mean ± SD. (Ctrl n=6, LCMV n=8, LPS n=15, C. Alb n=15; ****P<0.0001; Two-way ANOVA/ Holm-Sidak test). Representative confocal images from meningeal wholemounts show laminin staining in red, and functional vessels visualized with i.v. fluorescent tomato lectin in green. White dotted lines denote areas of injury and vascular repair. Scale bar, 200 μm. Source data in Source Data Extended Data Fig. 1.

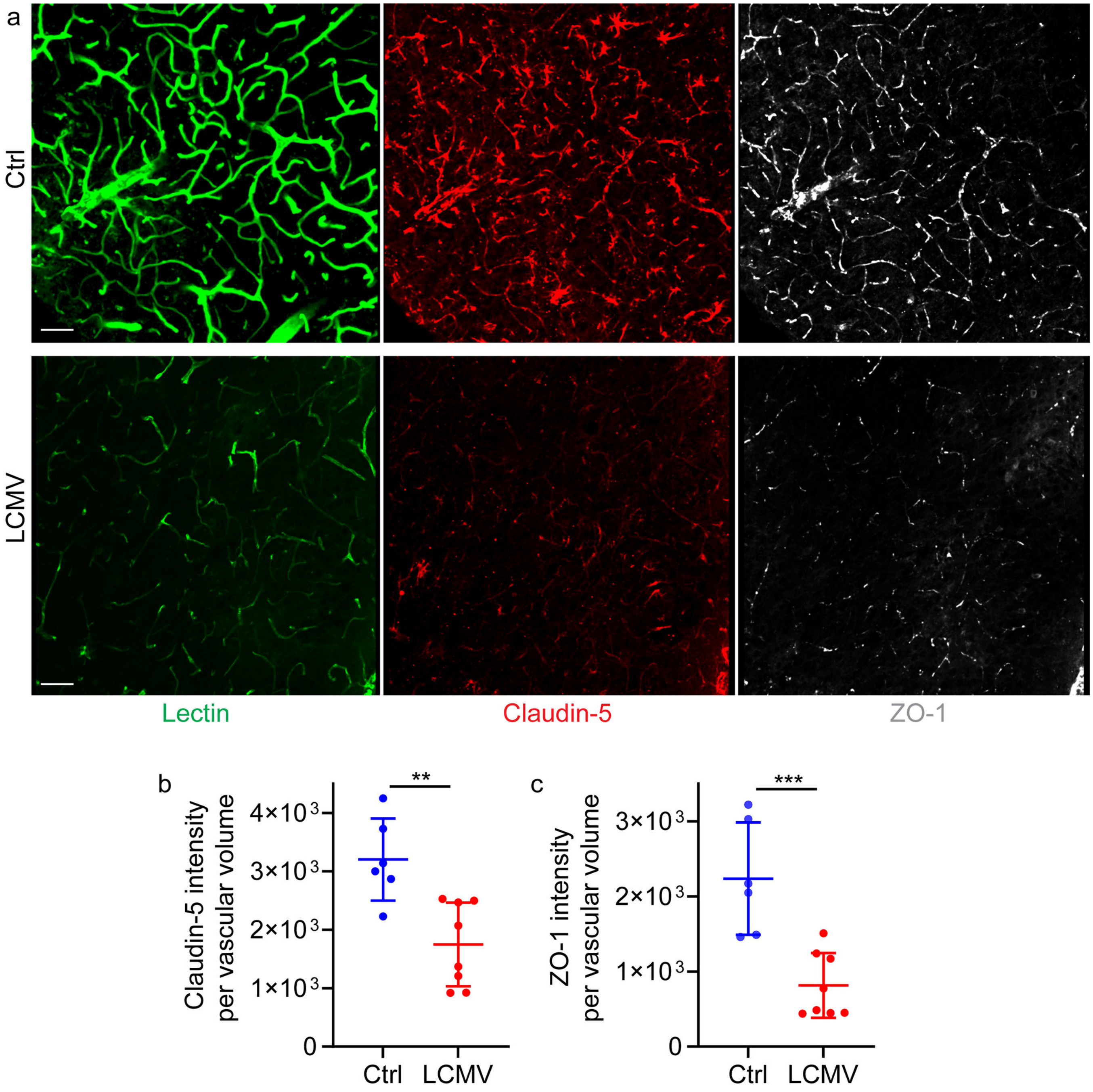

Extended Data Fig. 2. Viral infection after CVI reduces tight junction protein expression.

a. Axial confocal images show i.v. injected tomato lectin (green), claudin-5 (red) and ZO-1 (white) in the superficial neocortex of uninfected (Ctrl) and d4 LCMV-infected B6 mice at day 20 post-CVI. Scale bar, 50 µm. b, c. Dot plots show image-based quantification of claudin-5 (b) and ZO-1 (c) sum intensity per vascular volume. Data represent a compilation of two independent experiments. Each symbol represents an individual mouse and asterisks denote statistical significance. Data are represented as mean ± SD. (Ctrl n=6, LCMV n=8; **P<0.01, ***P<0.0001; Two-tailed Student's t-test). Source data for b,c in Source Data Extended Data Fig. 2.

Supplementary Material

Refer to Web version on PubMed Central for supplementary material.

Acknowledgements

This research was supported by the intramural program at the National Institute of Neurological Disorders and Stroke (NINDS), National Institutes of Health (NIH). We thank Abdel Elkahloun and Weiwei Wu in the National Human Genome Research Institute Microarray core for their assistance with the RNAseq experiment.

References

1. Capizzi A, Woo J & Verduzco-Gutierrez M Traumatic Brain Injury: An Overview of Epidemiology, Pathophysiology, and Medical Management. Med Clin North Am 104, 213–238, doi:10.1016/j.mcna.2019.11.001 (2020). [PubMed: 32035565]
2. Powers WJet al. Guidelines for the Early Management of Patients With Acute Ischemic Stroke: 2019 Update to the 2018 Guidelines for the Early Management of Acute Ischemic Stroke: A Guideline for Healthcare Professionals From the American Heart Association/American Stroke Association. Stroke50, e344–e418, doi:10.1161/STR.0000000000000211 (2019). [PubMed: 31662037]
3. Schumacher R, Muri RM & Walder B Integrated Health Care Management of Moderate to Severe TBI in Older Patients-A Narrative Review. Curr Neurol Neurosci Rep 17, 92, doi:10.1007/s11910-017-0801-7 (2017). [PubMed: 28986740]
4. Pendlebury ST & Rothwell PM Prevalence, incidence, and factors associated with pre-stroke and post-stroke dementia: a systematic review and meta-analysis. Lancet Neurol 8, 1006–1018, doi:10.1016/S1474-4422(09)70236-4 (2009). [PubMed: 19782001]
5. Nordstrom A & Nordstrom P Traumatic brain injury and the risk of dementia diagnosis: A nationwide cohort study. PLoS Med 15, e1002496, doi:10.1371/journal.pmed.1002496 (2018). [PubMed: 29381704]
6. Vermeij FHet al. Stroke-associated infection is an independent risk factor for poor outcome after acute ischemic stroke: data from the Netherlands Stroke Survey. Cerebrovasc Dis27, 465–471, doi:10.1159/000210093 (2009). [PubMed: 19329851]
7. Kourbeti ISet al. Infections in traumatic brain injury patients. Clin Microbiol Infect18, 359–364, doi:10.1111/j.1469-0691.2011.03625.x (2012). [PubMed: 21851488]
8. Lord ASet al. Infection after intracerebral hemorrhage: risk factors and association with outcomes in the ethnic/racial variations of intracerebral hemorrhage study. Stroke45, 3535–3542, doi:10.1161/STROKEAHA.114.006435 (2014). [PubMed: 25316275]
9. Sharma Ret al. Infections after a traumatic brain injury: The complex interplay between the immune and neurological systems. Brain Behav Immun79, 63–74, doi:10.1016/j.bbi.2019.04.034 (2019). [PubMed: 31029794]
10. Shim R & Wong CHY Complex interplay of multiple biological systems that contribute to post-stroke infections. Brain Behav Immun 70, 10–20, doi:10.1016/j.bbi.2018.03.019 (2018). [PubMed: 29571897]
11. Ritzel RMet al. Chronic Alterations in Systemic Immune Function after Traumatic Brain Injury. J Neurotrauma35, 1419–1436, doi:10.1089/neu.2017.5399 (2018). [PubMed: 29421977]

12. Harrison-Felix C, Whiteneck G, Devivo MJ, Hammond FM & Jha A Causes of death following 1 year postinjury among individuals with traumatic brain injury. J Head Trauma Rehabil 21, 22–33, doi:10.1097/00001199-200601000-00003 (2006). [PubMed: 16456389]
13. Kesinger MRet al. Hospital-acquired pneumonia is an independent predictor of poor global outcome in severe traumatic brain injury up to 5 years after discharge. J Trauma Acute Care Surg78, 396–402, doi:10.1097/TA.0000000000000526 (2015). [PubMed: 25757128]
14. Andraweera N & Seemann R Acute rehospitalisation during the first 3 months of in-patient rehabilitation for traumatic brain injury. Aust Health Rev 40, 114–117, doi:10.1071/AH15062 (2016). [PubMed: 26164449]
15. Westendorp WF, Nederkoorn PJ, Vermeij JD, Dijkgraaf MG & van de Beek D Post-stroke infection: a systematic review and meta-analysis. BMC Neurol 11, 110, doi:10.1186/1471-2377-11-110 (2011). [PubMed: 21933425]
16. Westendorp WFet al. The Preventive Antibiotics in Stroke Study (PASS): a pragmatic randomised open-label masked endpoint clinical trial. Lancet385, 1519–1526, doi:10.1016/S0140-6736(14)62456-9 (2015). [PubMed: 25612858]
17. Rico RM, Ripamonti R, Burns AL, Gamelli RL & DiPietro LA The effect of sepsis on wound healing. J Surg Res 102, 193–197, doi:10.1006/jsre.2001.6316 (2002). [PubMed: 11796018]
18. Koskela Met al. Epidermal wound healing in severe sepsis and septic shock in humans. Crit Care13, R100, doi:10.1186/cc7932 (2009). [PubMed: 19552820]
19. Jassam YN, Izzy S, Whalen M, McGavern DB & El Khoury J Neuroimmunology of Traumatic Brain Injury: Time for a Paradigm Shift. Neuron 95, 1246–1265, doi:10.1016/j.neuron.2017.07.010 (2017). [PubMed: 28910616]
20. Shlosberg D, Benifla M, Kaufer D & Friedman A Blood-brain barrier breakdown as a therapeutic target in traumatic brain injury. Nat Rev Neurol 6, 393–403, doi:10.1038/nrneurol.2010.74 (2010). [PubMed: 20551947]
21. Mastorakos P & McGavern D The anatomy and immunology of vasculature in the central nervous system. Sci Immunol 4, doi:10.1126/sciimmunol.aav0492 (2019).
22. Russo MV & McGavern DB Inflammatory neuroprotection following traumatic brain injury. Science 353, 783–785, doi:10.1126/science.aaf6260 (2016). [PubMed: 27540166]
23. Vannella KM & Wynn TA Mechanisms of Organ Injury and Repair by Macrophages. Annu Rev Physiol 79, 593–617, doi:10.1146/annurev-physiol-022516-034356 (2017). [PubMed: 27959618]
24. Shechter Ret al. Recruitment of beneficial M2 macrophages to injured spinal cord is orchestrated by remote brain choroid plexus. Immunity38, 555–569, doi:10.1016/j.immuni.2013.02.012 (2013). [PubMed: 23477737]
25. Roth TLet al. Transcranial amelioration of inflammation and cell death after brain injury. Nature505, 223–228, doi:10.1038/nature12808 (2014). [PubMed: 24317693]
26. Russo MV, Latour LL & McGavern DB Distinct myeloid cell subsets promote meningeal remodeling and vascular repair after mild traumatic brain injury. Nat Immunol 19, 442–452, doi:10.1038/s41590-018-0086-2 (2018). [PubMed: 29662169]
27. Mastorakos Pet al. Temporally distinct myeloid cell responses mediate damage and repair after cerebrovascular injury. Nat Neurosci24, 245–258, doi:10.1038/s41593-020-00773-6 (2021). [PubMed: 33462481]
28. Iadecola C & Anrather J The immunology of stroke: from mechanisms to translation. Nat Med 17, 796–808, doi:10.1038/nm.2399 (2011). [PubMed: 21738161]
29. Ahmed NAet al. Mechanisms for the diminished neutrophil exudation to secondary inflammatory sites in infected patients with a systemic inflammatory response (sepsis). Crit Care Med27, 2459–2468, doi:10.1097/00003246-199911000-00023 (1999). [PubMed: 10579265]
30. Santoro MM & Gaudino G Cellular and molecular facets of keratinocyte reepithelization during wound healing. Exp Cell Res 304, 274–286, doi:10.1016/j.yexcr.2004.10.033 (2005). [PubMed: 15707592]
31. Traub EPersistence of Lymphocytic Choriomeningitis Virus in Immune Animals and Its Relation to Immunity. J Exp Med63, 847–861, doi:10.1084/jem.63.6.847 (1936). [PubMed: 19870509]

32. Volkert M & Larsen JH Studies on Immunological Tolerance to Lcm Virus. 5. The Induction of Tolerance to the Virus. Acta Pathol Microbiol Scand 63, 161–171, doi:10.1111/apm.1965.63.2.161 (1965). [PubMed: 14295435]
33. Moseman EA, Blanchard AC, Nayak D & McGavern DB T cell engagement of cross-presenting microglia protects the brain from a nasal virus infection. Sci Immunol 5, doi:10.1126/sciimmunol.abb1817 (2020).
34. Fensterl V & Sen GC Interferons and viral infections. Biofactors 35, 14–20, doi:10.1002/biof.6 (2009). [PubMed: 19319841]
35. Zhou Set al. Induction and inhibition of type I interferon responses by distinct components of lymphocytic choriomeningitis virus. J Virol84, 9452–9462, doi:10.1128/JVI.00155-10 (2010). [PubMed: 20592086]
36. Gliem Met al. Macrophages prevent hemorrhagic infarct transformation in murine stroke models. Ann Neurol71, 743–752, doi:10.1002/ana.23529 (2012). [PubMed: 22718543]
37. Wattananit Set al. Monocyte-Derived Macrophages Contribute to Spontaneous Long-Term Functional Recovery after Stroke in Mice. J Neurosci36, 4182–4195, doi:10.1523/JNEUROSCI.4317-15.2016 (2016). [PubMed: 27076418]
38. Fenn AMet al. Immune activation promotes depression 1 month after diffuse brain injury: a role for primed microglia. Biol Psychiatry76, 575–584, doi:10.1016/j.biopsych.2013.10.014 (2014). [PubMed: 24289885]
39. Muccigrosso MMet al. Cognitive deficits develop 1month after diffuse brain injury and are exaggerated by microglia-associated reactivity to peripheral immune challenge. Brain Behav Immun54, 95–109, doi:10.1016/j.bbi.2016.01.009 (2016). [PubMed: 26774527]
40. Doran SJet al. Early or Late Bacterial Lung Infection Increases Mortality After Traumatic Brain Injury in Male Mice and Chronically Impairs Monocyte Innate Immune Function. Crit Care Med48, e418–e428, doi:10.1097/CCM.0000000000004273 (2020). [PubMed: 32149839]
41. Davis FMet al. Sepsis Induces Prolonged Epigenetic Modifications in Bone Marrow and Peripheral Macrophages Impairing Inflammation and Wound Healing. Arterioscler Thromb Vasc Biol39, 2353–2366, doi:10.1161/ATVBAHA.119.312754 (2019). [PubMed: 31644352]
42. Hazeldine J, Lord JM & Belli A Traumatic Brain Injury and Peripheral Immune Suppression: Primer and Prospectus. Front Neurol 6, 235, doi:10.3389/fneur.2015.00235 (2015). [PubMed: 26594196]
43. Angus DC & Opal S Immunosuppression and Secondary Infection in Sepsis: Part, Not All, of the Story. JAMA 315, 1457–1459, doi:10.1001/jama.2016.2762 (2016). [PubMed: 26975243]
44. Sadler AJ & Williams BR Interferon-inducible antiviral effectors. Nat Rev Immunol 8, 559–568, doi:10.1038/nri2314 (2008). [PubMed: 18575461]
45. McNab F, Mayer-Barber K, Sher A, Wack A & O’Garra A Type I interferons in infectious disease. Nat Rev Immunol 15, 87–103, doi:10.1038/nri3787 (2015). [PubMed: 25614319]
46. Amarante-Mendes GPet al. Pattern Recognition Receptors and the Host Cell Death Molecular Machinery. Front Immunol9, 2379, doi:10.3389/fimmu.2018.02379 (2018). [PubMed: 30459758]
47. Abdullah Aet al. STING-mediated type-I interferons contribute to the neuroinflammatory process and detrimental effects following traumatic brain injury. J Neuroinflammation15, 323, doi:10.1186/s12974-018-1354-7 (2018). [PubMed: 30463579]
48. Karve IPet al. Ablation of Type-1 IFN Signaling in Hematopoietic Cells Confers Protection Following Traumatic Brain Injury. eNeuro3, doi:10.1523/ENEURO.0128-15.2016 (2016).
49. Barrett JPet al. Interferon-beta Plays a Detrimental Role in Experimental Traumatic Brain Injury by Enhancing Neuroinflammation That Drives Chronic Neurodegeneration. J Neurosci40, 2357–2370, doi:10.1523/JNEUROSCI.2516-19.2020 (2020). [PubMed: 32029532]
50. Tsirogianni AK, Moutsopoulos NM & Moutsopoulos HM Wound healing: immunological aspects. Injury 37 Suppl 1, S5–12, doi:10.1016/j.injury.2006.02.035 (2006). [PubMed: 16616753]
51. Shi C & Pamer EG Monocyte recruitment during infection and inflammation. Nat Rev Immunol 11, 762–774, doi:10.1038/nri3070 (2011). [PubMed: 21984070]
52. Kenyon AJDelayed wound healing in mice associated with viral alteration of macrophages. Am J Vet Res44, 652–656 (1983). [PubMed: 6307086]

53. Crane MJet al. Pulmonary influenza A virus infection leads to suppression of the innate immune response to dermal injury. PLoS Pathog14, e1007212, doi:10.1371/journal.ppat.1007212 (2018). [PubMed: 30138446]
54. Erdur Het al. In-hospital stroke recurrence and stroke after transient ischemic attack: frequency and risk factors. Stroke46, 1031–1037, doi:10.1161/STROKEAHA.114.006886 (2015). [PubMed: 25737318]
55. McColl BW, Rothwell NJ & Allan SM Systemic inflammatory stimulus potentiates the acute phase and CXC chemokine responses to experimental stroke and exacerbates brain damage via interleukin-1- and neutrophil-dependent mechanisms. J Neurosci 27, 4403–4412, doi:10.1523/JNEUROSCI.5376-06.2007 (2007). [PubMed: 17442825]
56. Xiong Y, Mahmood A & Chopp M Angiogenesis, neurogenesis and brain recovery of function following injury. Curr Opin Investig Drugs 11, 298–308 (2010).
57. Krupinski J, Kaluza J, Kumar P, Kumar S & Wang JM Role of angiogenesis in patients with cerebral ischemic stroke. Stroke 25, 1794–1798, doi:10.1161/01.str.25.9.1794 (1994). [PubMed: 7521076]
58. Cumming TB & Brodtmann A Can stroke cause neurodegenerative dementia? Int J Stroke 6, 416–424, doi:10.1111/j.1747-4949.2011.00666.x (2011). [PubMed: 21951407]
59. Kraemer Met al. Delayed shrinkage of the brain after ischemic stroke: preliminary observations with voxel-guided morphometry. J Neuroimaging14, 265–272, doi:10.1177/1051228404264950 (2004). [PubMed: 15228769]
60. Nitkunan A, Lanfranconi S, Charlton RA, Barrick TR & Markus HS Brain atrophy and cerebral small vessel disease: a prospective follow-up study. Stroke 42, 133–138, doi:10.1161/STROKEAHA.110.594267 (2011). [PubMed: 21148440]
61. Gorelick PB & Nyenhuis D Stroke and Cognitive Decline. JAMA 314, 29–30, doi:10.1001/jama.2015.7149 (2015). [PubMed: 26151263]
62. Wardlaw JM, Sandercock PA, Dennis MS & Starr J Is breakdown of the blood-brain barrier responsible for lacunar stroke, leukoaraiosis, and dementia? Stroke 34, 806–812, doi:10.1161/01.STR.0000058480.77236.B3 (2003).
63. Rothenburg LSet al. The relationship between inflammatory markers and post stroke cognitive impairment. J Geriatr Psychiatry Neurol23, 199–205, doi:10.1177/0891988710373598 (2010). [PubMed: 20601647]
64. Kliper Eet al. Cognitive decline after stroke: relation to inflammatory biomarkers and hippocampal volume. Stroke44, 1433–1435, doi:10.1161/STROKEAHA.111.000536 (2013). [PubMed: 23444307]
65. Becker KJ, Kindrick DL, Lester MP, Shea C & Ye ZC Sensitization to brain antigens after stroke is augmented by lipopolysaccharide. J Cereb Blood Flow Metab 25, 1634–1644, doi:10.1038/sj.jcbfm.9600160 (2005). [PubMed: 15931160]

Method References

66. Clausen BE, Burkhardt C, Reith W, Renkawitz R & Forster I Conditional gene targeting in macrophages and granulocytes using LysMcre mice. Transgenic Res 8, 265–277, doi:10.1023/a:1008942828960 (1999). [PubMed: 10621974]
67. Prigge JRet al. Type I IFNs Act upon Hematopoietic Progenitors To Protect and Maintain Hematopoiesis during Pneumocystis Lung Infection in Mice. J Immunol195, 5347–5357, doi:10.4049/jimmunol.1501553 (2015). [PubMed: 26519535]
68. Gitlin Let al. Essential role of mda-5 in type I IFN responses to polyriboinosinic:polyribocytidylic acid and encephalomyocarditis picornavirus. Proc Natl Acad Sci U S A103, 8459–8464, doi:10.1073/pnas.0603082103 (2006). [PubMed: 16714379]
69. Jung Set al. Analysis of fractalkine receptor CX(3)CR1 function by targeted deletion and green fluorescent protein reporter gene insertion. Mol Cell Biol20, 4106–4114, doi:10.1128/mcb.20.11.4106-4114.2000 (2000). [PubMed: 10805752]

70. Saederup Net al. Selective chemokine receptor usage by central nervous system myeloid cells in CCR2-red fluorescent protein knock-in mice. PLoS One5, e13693, doi:10.1371/journal.pone.0013693 (2010). [PubMed: 21060874]
71. Muller Uet al. Functional role of type I and type II interferons in antiviral defense. Science264, 1918–1921, doi:10.1126/science.8009221 (1994). [PubMed: 8009221]
72. Manglani M & McGavern DB Intravital Imaging of Neuroimmune Interactions Through a Thinned Skull. Curr Protoc Immunol 120, 24 22 21–24 22 12, doi:10.1002/cpim.46 (2018).
73. Oldstone MB, Blount P, Southern PJ & Lampert PW Cytoimmunotherapy for persistent virus infection reveals a unique clearance pattern from the central nervous system. Nature 321, 239–243, doi:10.1038/321239a0 (1986). [PubMed: 3086743]
74. Welsh RM & Seedhom MO Lymphocytic choriomeningitis virus (LCMV): propagation, quantitation, and storage. Curr Protoc Microbiol Chapter 15, Unit 15A 11, doi:10.1002/9780471729259.mc15a01s8 (2008).
75. Navarathna DHet al. Enhanced pathogenicity of Candida albicans pre-treated with subinhibitory concentrations of fluconazole in a mouse model of disseminated candidiasis. J Antimicrob Chemother56, 1156–1159, doi:10.1093/jac/dki383 (2005). [PubMed: 16239285]

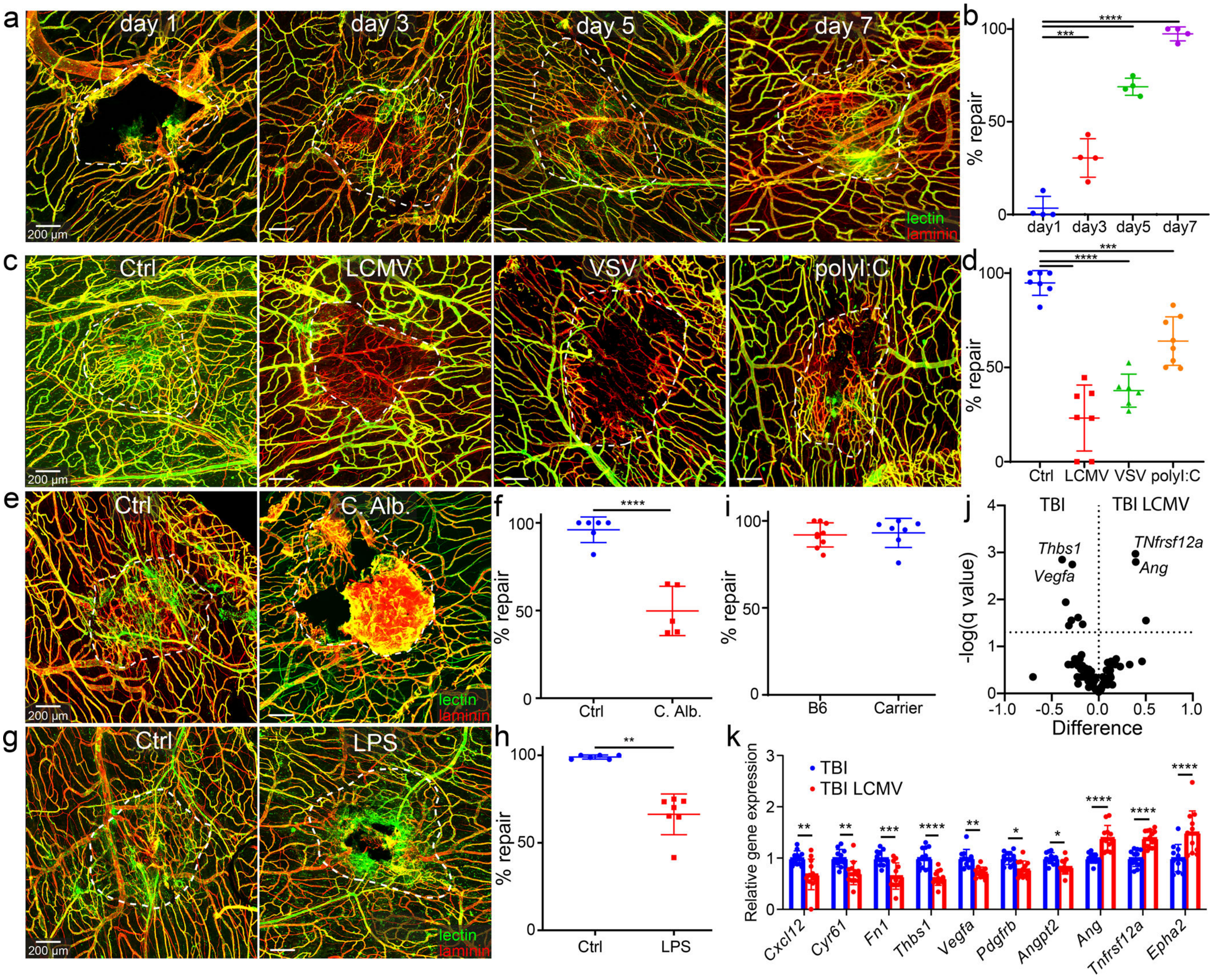

Figure 1. Systemic infections and PAMPs impede meningeal vascular repair following mTBI.

a, c, e, g. Representative confocal images of meningeal whole mounts show vascular damage and repair in mice after mTBI. Blood vessels are labeled with anti-laminin staining (red) and intravenous (i.v.) fluorescent Tomato lectin (green). The white dotted lines delineate the area of injury and vascular repair. Scale bar, 200 µm. **b, d, f, h, i.** Dot plots show quantification of percent lesion repair (mean ± SD). Each symbol represents an individual mouse, and asterisks denote statistical significance (***P ≤ 0.001, ****P ≤ 0.0001; b,d One-way ANOVA/Tukey test; f,i Two-tailed Student's t-test; Two-tailed h Two-tailed Mann–Whitney U test). Data are representative of two independent experiments. **a, b.** Area of injury and repair on days 1, 3, 5, and 7 post-mTBI (n=4 mice per group). **c, d.** Area of injury and repair 7 days after mTBI relative to unchallenged controls (Ctrl) decreased repair was observed following injection of LCMV i.v., VSV intranasally, or poly I:C i.v. (Ctrl, LCMV n=7, VSV n=6, polyI:C n=8 mice). **e, f.** Images captured d7 post-TBI show decreased repair in mice injected i.v. with *Candida albicans* relative to Ctrl (Ctrl n=6, *C. Alb.* n=5 mice). **g, h.** Meningeal images d7 post-TBI depict decreased repair in mice injected i.v. with LPS relative to Ctrl (Ctrl n=6, LPS n=7 mice per group). i. Quantification of repair demonstrates complete repair of LCMV carrier mice relative to Ctrl (B6 n=9, Carrier n=7 mice). **j, k.** Quantification of angiogenesis-related gene expression by qPCR in the injured meninges and superficial neocortex from uninfected and d4 LCMV-infected mice on d5 post-injury. Data are a compilation of two independent experiments (TBI n=11, TBI LCMV n=12 mice). Volcano plot showing differential expression (double delta Ct analysis, δδCt) of 88 genes related to angiogenesis. Statistical analysis was performed using multiple Two-tailed t-tests and the Benjamini, Krieger and Yekutieli method to correct for the false discovery rate, with a desired Q value of 5% (dotted line) (**j**). Bar graph showing relative gene expression (δδCt) with Q value of less than 5% (mean ± SD) (**k**). Each symbol represents an individual mouse, and asterisks denote statistical significance (*P ≤ 0.05, **P ≤ 0.01, ***P ≤ 0.001, ****P ≤ 0.0001; Two-way ANOVA/Holm-Sidak test). Source data for j, k in Supplementary Table 1a and for b, d, f, h, i in Source Data Fig. 1. Statistical analysis in Supplementary Table 5.

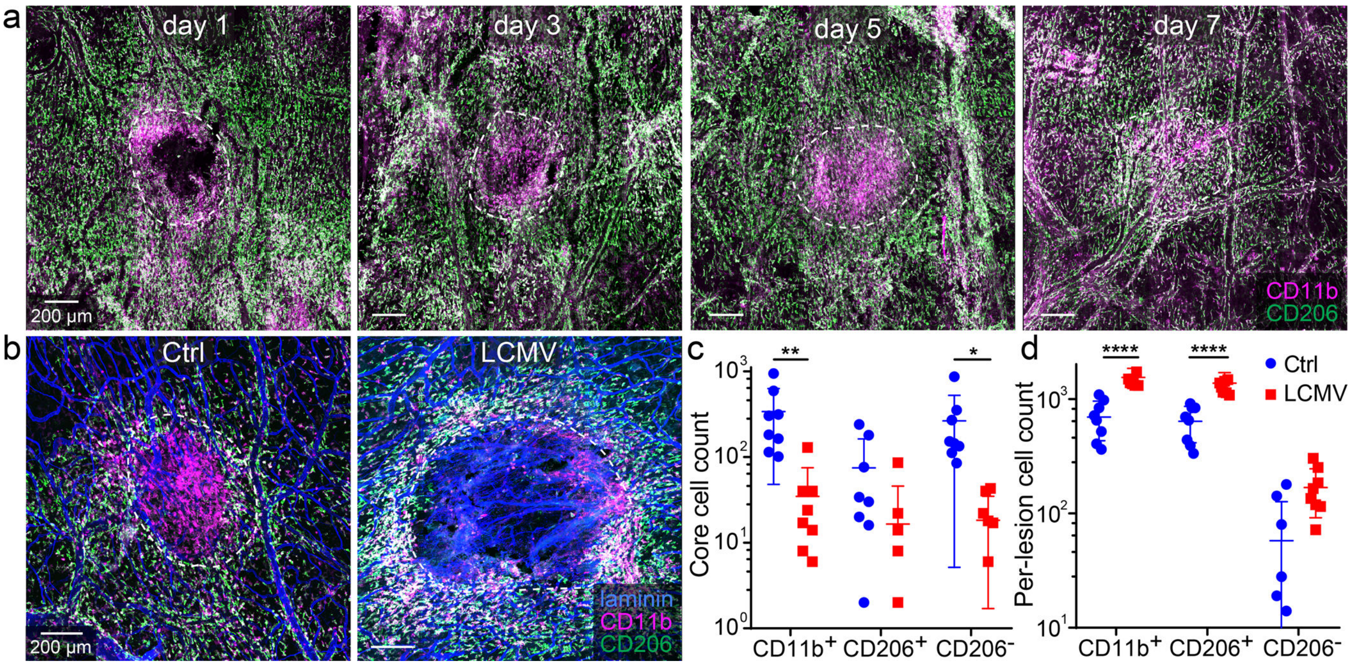

Figure 2. LCMV infection alters the distribution of myeloid cells in lesion core and perimeter.

a. Confocal images of meningeal whole mounts show the distribution of CD11b+ (pink) and CD206+ (green) myeloid cells in the lesion and perilesional area at d1, d3, d4, and d7 post-mTBI. Lesions are delineated with dotted white lines. Scale bar, 200 µm. White: overlap **b.** Representative confocal images from meningeal whole mounts show lesion and peri-lesion CD11b+ (pink) and CD206+ (green) myeloid cells at day 5 post-mTBI in uninfected and d4 i.v. LCMV-infected mice. Laminin staining is colored blue. Scale bar: 200 µm. **c, d.** Dot plots show quantification of CD11b+, CD11b+CD206+ (wound healing macrophages) and CD11b+CD206- (inflammatory macrophages) in the lesion (c) and peri-lesion (d) area. Data are representative of two independent experiments (n=8 mice per group). Data are represented as mean ± SD. In panel d, two samples do not appear on the graph for CD206- cells in the uninfected group because the cell count for both samples is zero and the scale on the *y*-axis is logarithmic. Each symbol represents an individual mouse, and asterisks denote statistical significance (**P ≤ 0.01, ****P ≤ 0.0001; Two-way ANOVA/Holm-Sidak test). Source data for c, d in Source Data Fig. 2. Statistical analysis in Supplementary Table 5.

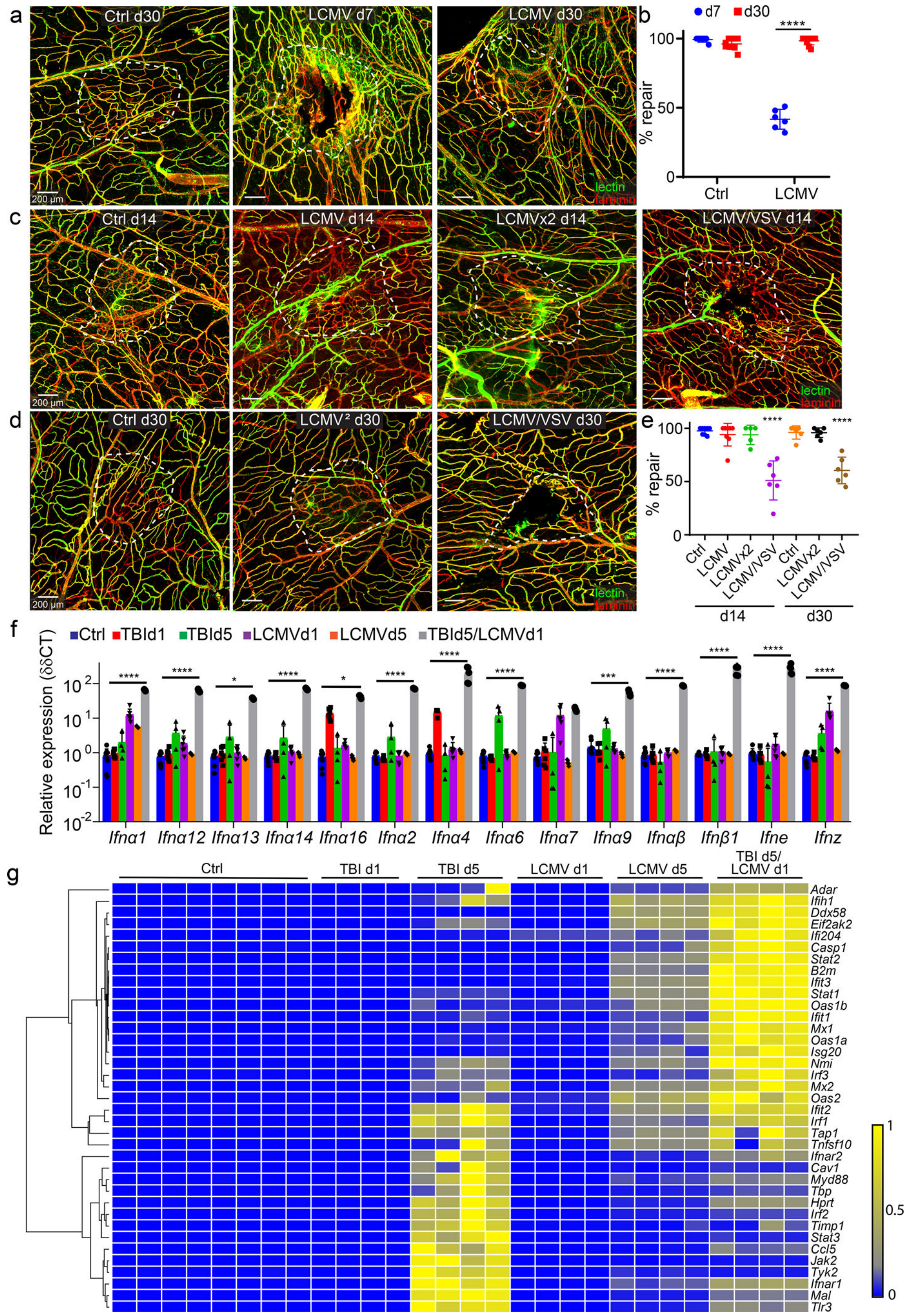

Figure 3. Infections induce a prolonged state of disrepair and interferon signaling in the meninges following mTBI.

a, c, d. Confocal microscopy images from meningeal wholemounts show laminin staining in red, and functional vessels visualized with i.v. fluorescent tomato lectin in green. White dotted lines denote areas of injury and vascular repair. Scale bar, 200 µm. **b, e**. Dot plots show quantification of percent lesion repair (mean ± SD). Each symbol represents an individual mouse. Data are representative of two independent experiments **a, b.** Areas of injury and repair day 7 and 30 post-mTBI, with or without i.v. LCMV. (d7 n=6, Ctrl d30 n=8, LCMV d30 n=10; ****P < 1e-15; Two-way ANOVA/Holm-Sidak test). **c-e.** Areas of injury and repair on days 14 and 30 post-mTBI. Uninfected (Ctrl) mice and mice infected i.v. with LCMV on day 4, or days 5 and 10 (LCMVx2), demonstrate near complete lesion repair on days 14 and 30 post-mTBI. Mice infected with LCMV i.v. on day 4 and intranasally with VSV on day 10 show incomplete repair on days 14 and 30 (Ctrl, LCMV n=8, other groups n=6; ****P ≤ 0.0001 compared to Ctrl; One-way ANOVA/Tukey test). **f.** Dot plot depicting qPCR analysis of relative type I interferon gene expression (δδCT) in punch biopsies of meninges and superficial neocortex. Mice underwent mTBI followed by i.v. LCMV infection on day 4 and quantification of gene expression on day 5 (TBI d5 / LCMV d1, n=5). Gene expression was compared to uninfected/uninjured mice (Ctrl, n=6), uninfected mice day 1 (TBI d1, n=6) and day 5 (TBI d5, n=4) after mTBI as well as i.v. LCMV mice on day 1 (LCMV d1, n=6) and day 5 (LCMV d5, n=5) post-infection. Each symbol represents an individual mouse. Data are represented as mean ± SD. Data represent two independent experiments. (**P ≤ 0.01, ****P ≤ 0.0001; Two-way ANOVA/Holm-Sidak test). **g.** Heatmap depicting qPCR analysis of type I interferon signaling related genes that were significantly increased (P < 0.005) based on two-way ANOVA/Holm-Šídák multiple comparison method. Groups are the same as those shown in panel f. Data are representative of two independent experiments (n=4 mice per group, Ctrl n=8). Source data for b, e in Source Data Fig. 3 and for f, g in Supplementary Tables 1b, c. Statistical analysis in Supplementary Table 5.

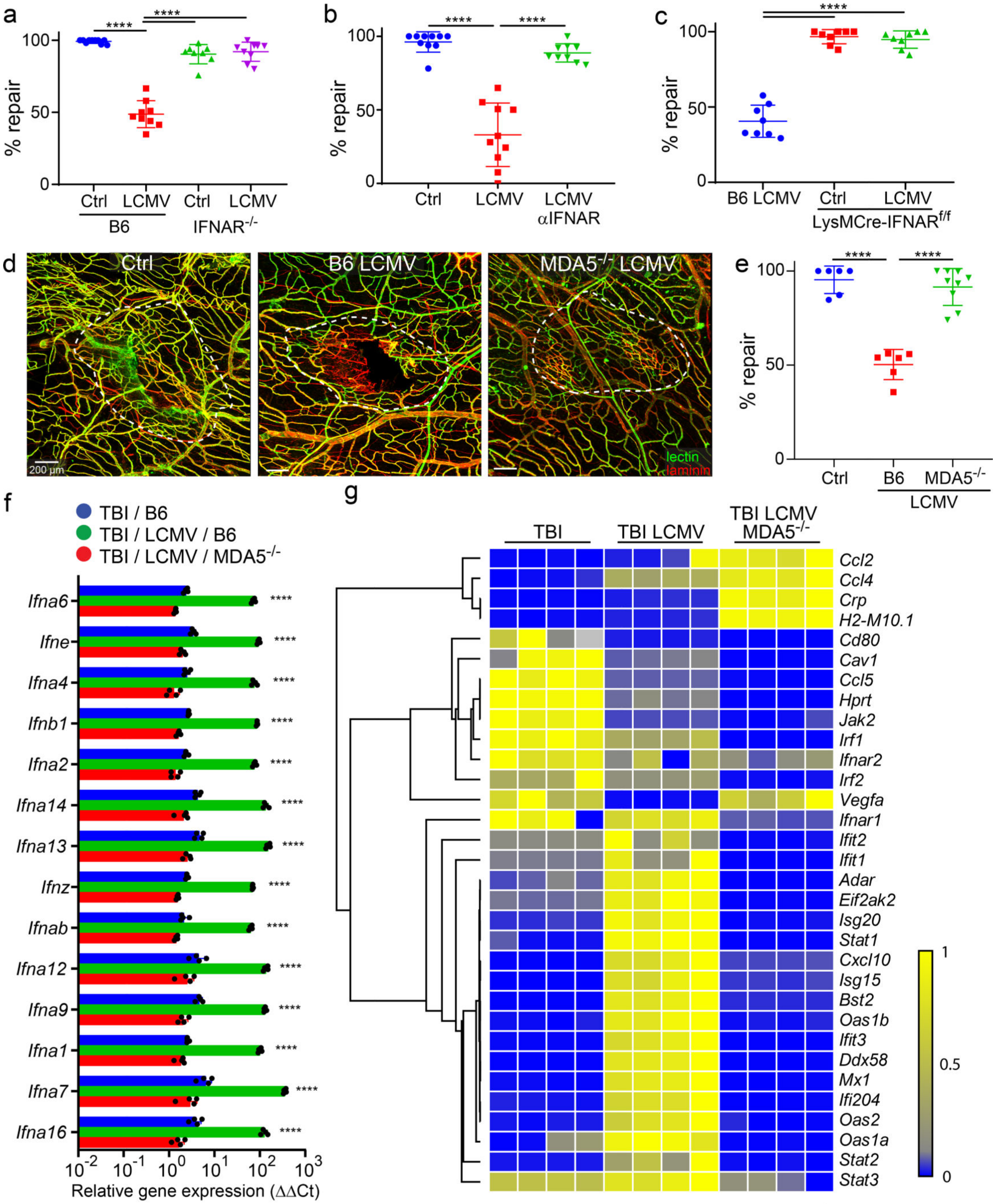

Figure 4. Deletion of pathogen sensing or interferon signaling reconstitutes meningeal repair after mTBI.

a. Dot plot shows quantification of percent lesion repair (mean ± SD) 7 days after mTBI in uninfected B6 (n=10) and and IFNAR$^{-/-}$ (n=8) mice versus LCMV i.v. infected B6 (n=9) and IFNAR$^{-/-}$ (n=9) mice. **b.** Dot plot shows percent lesion repair 7 days after mTBI in uninfected mice (n=10), LCMV infected mice (n=10), and LCMV infected mice + αIFNAR antibody (n=9). **c.** Dot plot shows percent lesion repair 7 days after mTBI in LCMV infected B6 mice as well as uninfected and infected LysMCre-IFNAR$^{f/f}$ mice (n=8 per group). **d.**

Confocal images show vascular damage and repair in uninfected B6 mice as well as LCMV-infected B6 and MDA5$^{-/-}$ mice at day 7 post-mTBI. The white dotted lines delineate areas of injury and repair. Fluorescent tomato lectin (green); laminin (red); Scale bar, 200 μm. **e.** Dot plot shows quantification of percent lesion repair (mean ± SD) for the groups in panel d. (Ctrl, B6 LCMV n=6, MDA5$^{-/-}$ LCMV n=9 mice). **f.** Dot plot depicting qPCR analysis of relative IFN-I gene expression (δδCT) in punch biopsies of meninges and superficial neocortex at day 7 post-mTBI for uninfected B6 mice as well as day 4 LCMV-infected B6 and MDA5$^{-/-}$ mice. Data are representative of two independent experiments 4 and 5 mice per group. **g.** Heatmap depicting qPCR analysis of type I interferon signaling related genes that were significantly increased (P<0.005) based on two-way ANOVA followed by the Holm-Šídák multiple comparison method. Groups are the same as those shown in panel F. Data are representative of two independent experiments with 4 and 5 mice per group. **a, b, c, e, f.** Data are representative of two independed experiments. Each symbol represents an individual mouse and asterisks denote statistical significance. Data are represented as mean ± SD. (****P ≤ 0.0001; a, b, c, e One-way ANOVA/Tukey test; f, g Two-way ANOVA/Holm-Sidak test). Source data for a, b, c, e in Source Data Fig. 4 and for f, g in Supplementary Tables 1d, e. Statistical analysis in Supplementary Table 5.

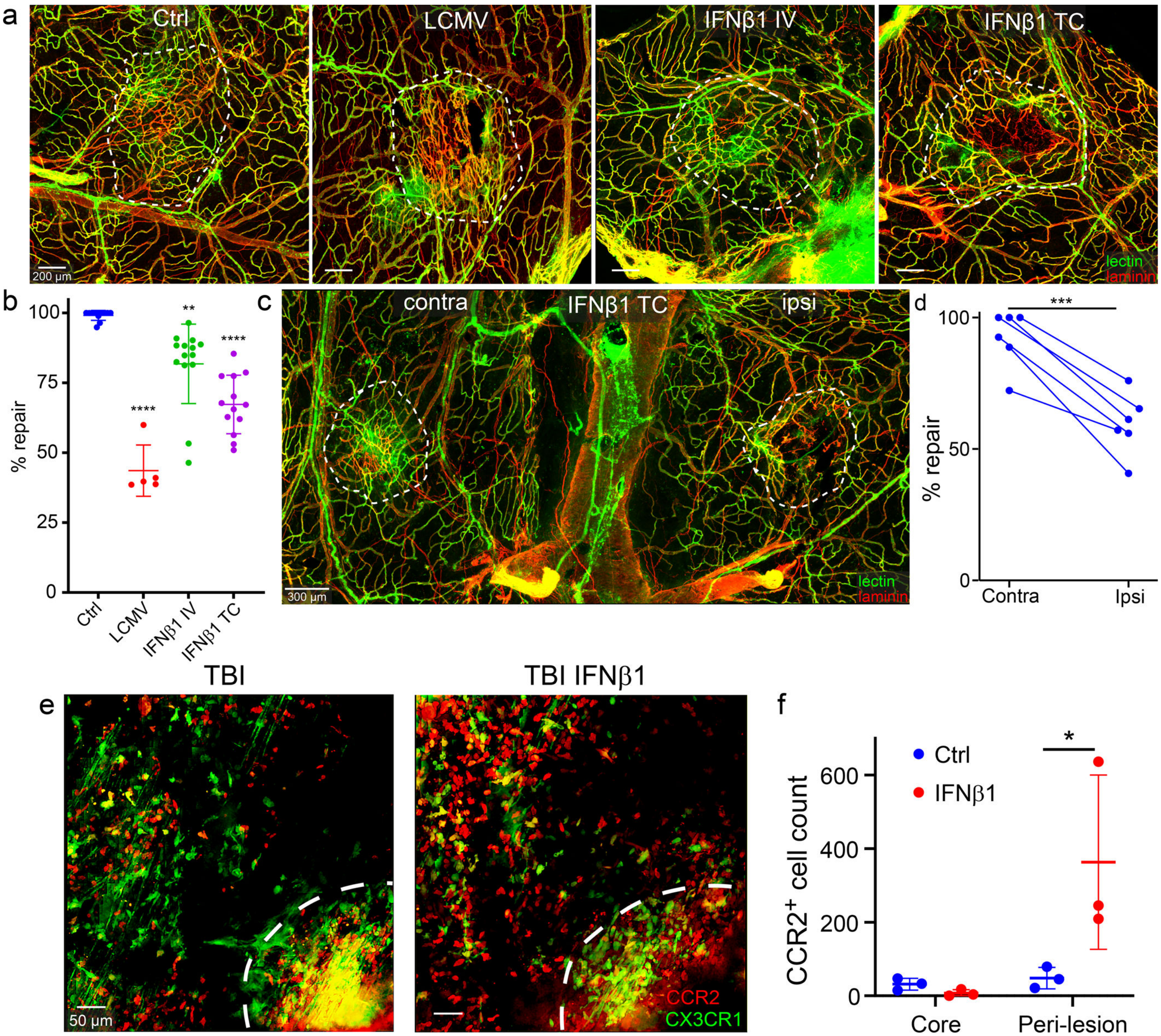

Figure 5. Transcranial application of IFNβ1 impedes meningeal vascular repair after mTBI.

a. Meningeal wholemount images depict areas of injury and repair at day 7 post-mTBI following intravenous (IV) or transcranial (TC) administration of IFNβ1 on days 5 and 6. Repair was compared to vehicle control treated B6 mice (Ctrl) as well as d4 LCMV-infected mice. The white dotted lines delineate areas of injury and repair. Fluorescent tomato lectin (green); laminin (red); Scale bar, 200 μm. **b.** Dot plot shows quantification of percent lesion repair (mean ± SD) for the groups in panel a. Data are the compilation of 2 independent experiments. Each symbol represents an individual mouse, and asterisks denote statistical significance (Ctrl n=11, LCMV n=5, IFNβ1IV n=14, IFNβ1TC n=13; **P ≤ 0.01, ****P ≤ 0.0001 compared to Ctrl; One-way ANOVA/Tukey test) relative to the control group. **c.** The meningeal wholemount image shows a bilateral injury and repair paradigm at day 7 post-mTBI. IFNβ1 (ipsilateral) or vehicle (contralateral) was administered transcranially

(TC) on days 5 and 6 post-mTBI. The white dotted lines delineate areas of injury and repair. Fluorescent tomato lectin (green); laminin (red); Scale bar, 200 μm. **d.** Dot plot shows quantification of percent lesion repair (mean ± SD) for the groups in panel C. Each symbol corresponds to an individual mouse, and connected dots represent ipsilateral and contralateral lesion of the same mouse. Data are a compilation of 2 independent experiments with 3 mice per group. Asterisks denote statistical significance (***P = 0.001; Two-tailed Paired t-test). **e.** Representative intravital two-photon microscopy images captured in the meninges of CX3CR1$^{gfp/wt}$CCR2$^{rfp/wt}$ mice demonstrate the lesion core (white dash line) and perilesional area 5 days following mTBI (left) and 90 minutes after transcranial IFNβ1 administration (right). CX3CR1 (green); CCR2 (red); Scale bar, 50 μm. **f.** Dot plot shows quantification of CCR2$^+$ monocytes in the lesion core and peri-lesion for the groups in panel e. Data represent 2 independent experiments with 3 mice per group. Each symbol represents an individual mouse, and asterisks denote statistical significance. Data are represented as mean ± SD. (*$P \leq 0.05$; Two-way ANOVA/Holm-Sidak test). Source data for b, d, f in Source Data Fig. 5. Statistical analysis in Supplementary Table 5.

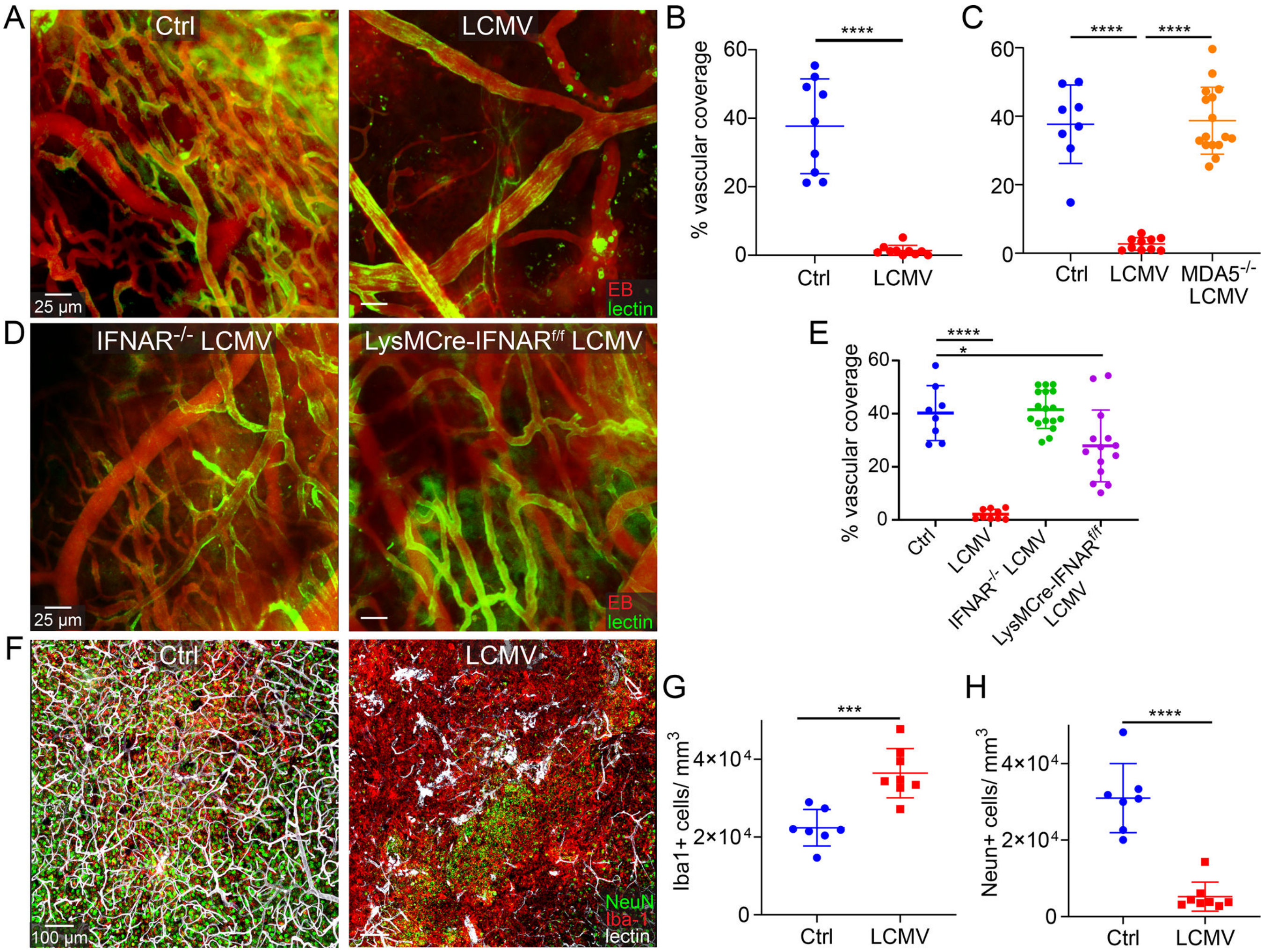

Figure 6. Viral infection and subsequent interferon signaling blocks angiogenesis after cerebrovascular injury.

a-e. Intravital 2-photon microscopy of cerebral cortical vasculature and image-based quantification of vascular coverage at day 10 post-cerebrovascular injury (CVI). Fluorescent tomato lectin (green) and Evans blue (red, EB) were injected i.v. prior to imaging. Scale bar, 25 μm. **a.** Representative images show parenchymal vasculature in the neocortex of uninfected and LCMV-infected B6 mice at day 10 post-CVI. **b.** Dot plot shows quantification of vascular coverage for the groups in panel a (Ctrl n=9, LCMV n=10). **c.** Dot plot depicts quantification of parenchymal vascular coverage at day 10 post-CVI in uninfected B6 mice (Ctrl) as well LCMV-infected B6 and MDA5$^{-/-}$ mice (Ctrl n=8, LCMV n=10, MDA5$^{-/-}$ LCMV n=16). **d.** Representative two-photon images show vascular coverage at day 10 post-CVI in day 4 LCMV-infected IFNAR$^{-/-}$ and LysMCre-IFNAR$^{f/f}$ mice. **e**. Dot plot shows quantification of vascular coverage at day 10 post-CVI for uninfected B6 mice (Ctrl) as well as day 4 LCMV-infected B6, IFNAR$^{-/-}$, and LysMCre-IFNAR$^{f/f}$ mice (Ctrl =8, LCMV n=9, IFNAR$^{-/-}$ LCMV n=17, LysMCre-IFNAR$^{f/f}$ LCMV n=14). **f.** Representative confocal microscopy images of neocortex at day 10 post-CVI show NeuN^{+} neurons (green), Iba-1^{+} myeloid cells (red), and fluorescent tomato lectin labeled blood vessels (white) for uninfected (Ctrl) and d4 LCMV-infected B6 mice. Scale bar, 100 μm. **g, h.** Dot plots demonstrate image-based quantification of Iba1$^+$ myeloid cells (g) and NeuN$^+$ neurons (h). (Ctrl n=7, LCMV n=8). **b, c, e, g, h**. Data are represented as mean ± SD and are a compilation of two independent experiments. Each symbol represents an individual mouse, and asterisks denote statistical significance (***P ≤ 0.001, ****P ≤ 0.0001; c, e One-way ANOVA/Tukey test; b, g, h Two-tailed Student's t-test). Source data for b, c, e, g, h in Source Data Fig. 6. Statistical analysis in Supplementary Table 5.

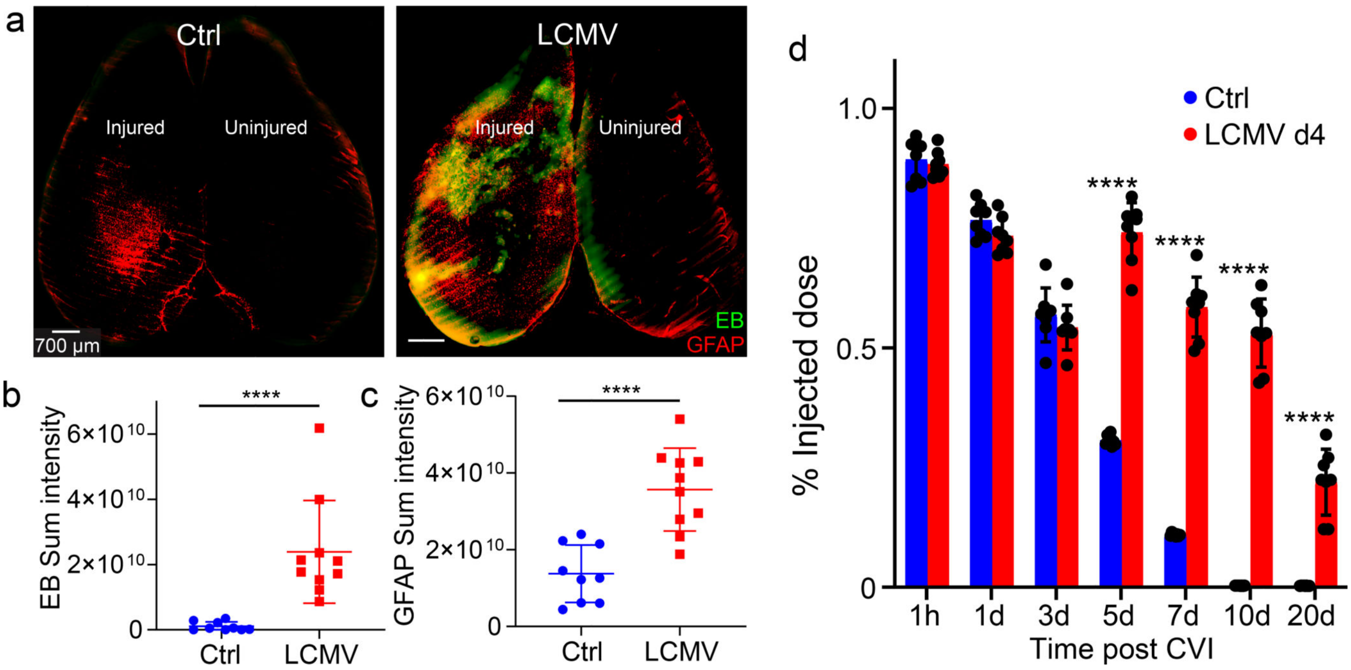

Figure 7. Viral infection and subsequent interferon signaling blocks BBB repair after CVI.

a. Axial confocal images show i.v. injected Evans blue (green, EB) and GFAP$^+$ astrocytes (red) in the superficial neocortex of uninfected (Ctrl) and d4 LCMV-infected B6 mice at day 10 post-CVI. Scale bar, 700 μm. **b, c.** Dot plots show image-based quantification of Evans blue (B) and GFAP (C) sum intensities. Data represent a compilation of two independent experiments (Ctrl n=9, LCMV n=10). **d.** Dot plot depicts quantification of fluorescein extravasation in the brains of uninfected (Ctrl) and day 4 LCMV-infected B6 mice at 1h, 1d, 3d, 5d, 7d, 10d and 20d post-CVI. Data represent 2 independent experiments with 8 mice per group. **b, c, d.** Each symbol represents an individual mouse, and asterisks denote statistical significance. Data are represented as mean ± SD. (****P ≤ 0.0001; b, c Two-tailed Student's t-test; d Two-way ANOVA/Holm-Sidak test). Source data for b, c, d in Source Data Fig. 7. Statistical analysis in Supplementary Table 5.

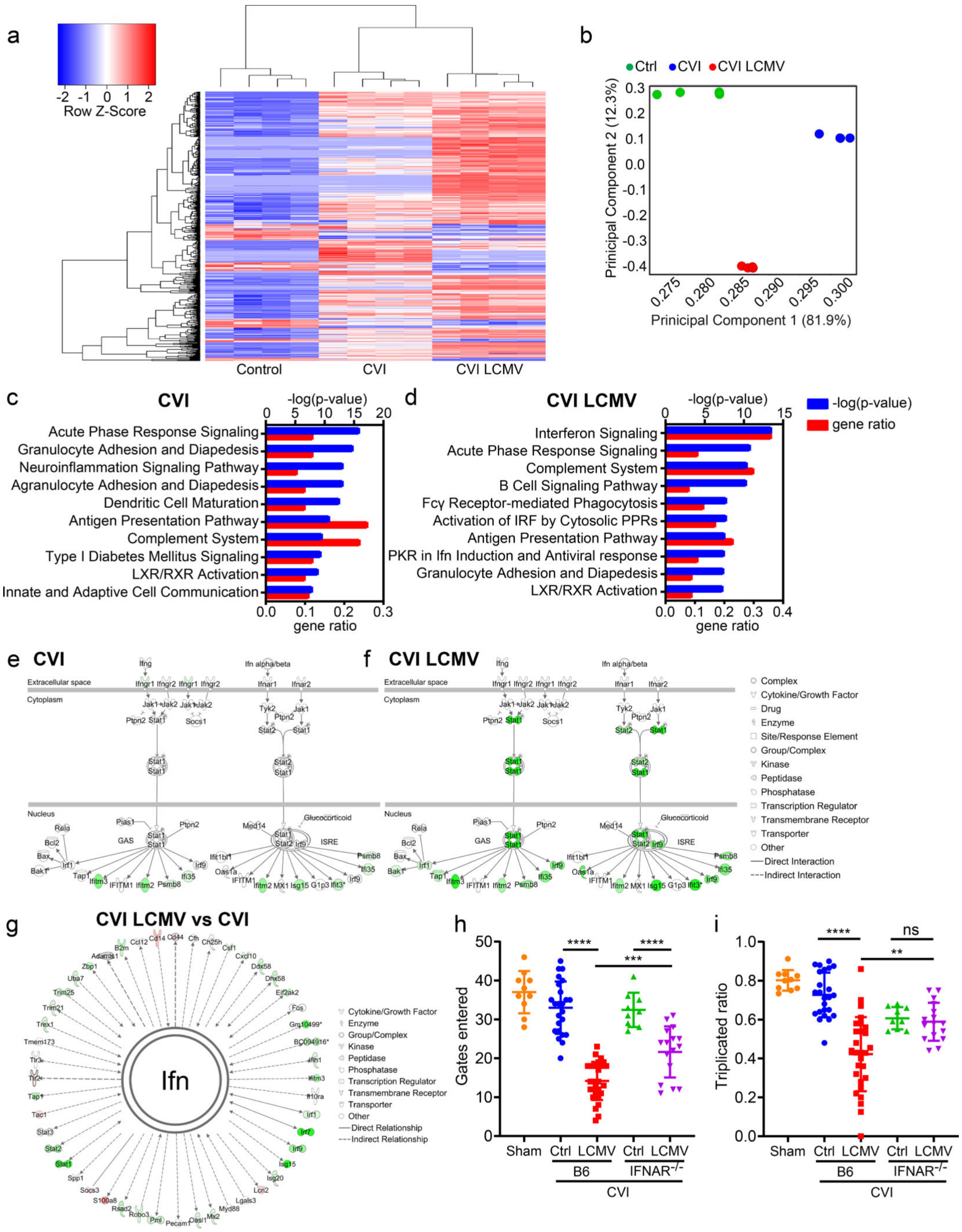

Figure 8. Viral infection after CVI leads to chronic interferon signaling and a failure to recover cognitive-motor function.

a-g. RNA sequencing analysis of gene expression in the cerebral cortex of uninjured mice (Ctrl) as well as uninfected (CVI) and d4 LCMV-infected B6 mice (CVI LCMV) at day 10 post-CVI (n=4 per group). **a.** A Pearson correlation-based clustered heat map shows the unique union of genes deemed to have a significant difference of expression between at least two classes. **b.** Covariance-based PCA scatterplot shows separate clustering of the different groups. Each dot represents individual mouse. **c, d.** Bar graphs demonstrate the p-value and upregulated gene ratio of 10 enriched pathways with the lowest enrichment p-value for CVI vs Ctrl mice (c) and CVI LCMV vs Ctrl mice mice (d). **e, f.** Ingenuity software based canonical pathway view of interferon signaling related genes in CVI vs Ctrl mice (e) and CVI LCMV vs Ctrl mice (f). Upregulated genes are shown in shades of green. **g.** A custom network view of all genes directly (solid lines) and indirectly (dotted lines) associated with interferon (Ifn) in CVI LCMV vs CVI mice. Upregulated genes are shown in shades of green and downregulated genes in shades of red. Source data and Ingenuity analysis analysis for a-g in Supplementary Tables 2–4. h, i. Dot plots show quantification of cognitive-motor function by Y-maze at day 20 after CVI in uninfected (Ctrl) and d4 LCMV-infected (LCMV), B6 and IFNAR$^{-/-}$ mice. The number of gates entered (h) and the triplicate ratio (i) are plotted. Cumulative data from four independent experiments. Each symbol represents an individual mouse and asterisks denote statistical significance. Data are represented as mean ± SD. (Sham n=10, Ctrl B6 n=24, LCMV B6 28, Ctrl IFNAR$^{-/-}$ 9, LCMV IFNAR$^{-/-}$ 16; **P<0.01, ***P<0.001, ****P<0.0001; Two-way ANOVA/ Holm-Sidak test). Source data for h, i in Source Data Fig. 8. Statistical analysis in Supplementary Table 5.